

Spectroscopy at the solar limb: II. Are spicules heated to coronal temperatures ?

C. Beck¹ · R. Rezaei² · K. G. Puschmann³ ·
D. Fabbian^{4,5,6}

© Springer

Abstract

Spicules of the so-called type II were suggested to be relevant for coronal heating because of their ubiquity on the solar surface and their eventual extension into the corona. We investigate whether solar spicules are heated to transition-region or coronal temperatures and reach coronal heights ($\gg 6$ Mm) using multi-wavelength observations of limb spicules in different chromospheric spectral lines (Ca II H, H ϵ , H α , Ca II IR at 854.2 nm, He I at 1083 nm) taken with slit-spectrographs and imaging spectrometers. We determine the line width of spectrally resolved line profiles in individual spicules and throughout the field of view and estimate the maximal height that different types of off-limb features reach. We derive estimates of the kinetic temperature and the non-thermal velocity from the line width of spectral lines from different chemical elements. We find that most regular – i.e., thin and elongated – spicules reach a maximal height of about 6 Mm above the solar limb. The majority of features found at larger heights are irregularly shaped with a significantly larger lateral extension – of up to a few Mm – than spicules. Both individual and average line profiles in all spectral lines show a decrease in their line width with height above the limb with very few exceptions. Both the kinetic temperature and the non-thermal velocity decrease with height above the limb. We find no indications that the spicules in our data reach coronal heights or transition-region or coronal temperatures.

Keywords: Sun: chromosphere – techniques: spectroscopic – line: profiles

¹: National Solar Observatory (NSO), 88349 Sunspot, New Mexico, USA cbeck@nso.edu

²: Kiepenheuer-Institut für Sonnenphysik (KIS), 79104 Freiburg, Germany

³: Martinstr. 64, 64285 Darmstadt, Germany

⁴: Instituto de Astrofísica de Canarias (IAC), 38205 La Laguna, Tenerife, Spain

⁵: Departamento de Astrofísica, Universidad de La Laguna (ULL), 38206 La Laguna, Tenerife, Spain

⁶: Max-Planck-Institut für Sonnensystemforschung (MPS), 37077 Göttingen, Germany

1. Introduction

Most of the processes on the solar surface, with the exception of the convective energy transport and solar oscillations, are driven by magnetic fields. At the photospheric level, the gas density is high enough to make the kinetic pressure dominant over the magnetic pressure. In contrast, the magnetic energy density is larger than the kinetic one in the chromosphere and the corona. Whereas the spatial structuring in the photosphere is given by the granulation pattern, the shape of the solar chromosphere is markedly different. One key component of the chromosphere are the so-called spicules: hair-like, thin, elongated features observed at the solar limb in strong chromospheric lines such as $H\alpha$ (e.g., Roberts 1945 or the reviews of Beckers 1968 (BE68), Sterling 2000 and Tsiropoula *et al.* 2012). Some spicules are bright in extreme ultraviolet (EUV) lines as well as in $H\alpha$, indicating an extension up to coronal heights. Spicules are transient features that apparently shoot up from the solar limb to a height of a few Mm (e.g., Zirker 1962b), to disappear from sight again after some tens of seconds to a few minutes (BE68; De Pontieu *et al.* 2007b). Because of possible projection effects, it is not clear if the apparent motions seen at the limb are caused by mass motions or waves. There are controversial observational arguments whether spicules fade away *in situ* or return to the solar surface (Suematsu, Wang, and Zirin 1995; Pasachoff, Jacobson, and Sterling 2009; Sterling, Moore, and DeForest 2010; Anan *et al.* 2010; Pereira, De Pontieu, and Carlsson 2012; Zhang *et al.* 2012). Pasachoff, Noyes, and Beckers (1968) and De Pontieu *et al.* (2012) suggested that spicules undergo twisting and torsional motions while they evolve.

On the solar disc, dark and bright mottles and fibrils are believed to be the counterpart of limb spicules (Beckers 1972). There is no canonical proof that mottles or fibrils are spicules seen on-disc, but they should at least be related (Grossmann-Doerth and Schmidt 1992; Tsiropoula and Schmieder 1997; Suematsu 1998; Zachariadis *et al.* 1999; Langangen *et al.* 2008; Rouppe van der Voort *et al.* 2009). Mottles cluster at the boundary of supergranular cells. The most reliable identification of the on-disc counterpart of spicules is through the corresponding line-of-sight (LOS) velocities (e.g., Sekse, Rouppe van der Voort, and De Pontieu 2012, 2013). There is no agreement if there are any spicules over plage regions (Shibata and Suematsu 1982; Zirin 1988; De Pontieu *et al.* 2007b, but see also Anan *et al.* 2010).

The typical length of spicules is from 5–10 Mm, while their width ranges from 1 Mm down to the resolution limit of the respective observations, i.e., as small as $0''.1$ (Beckers 1972; Nishikawa 1988; Suematsu *et al.* 2007, 2008). Hence, the aspect ratio of the hair-like spicular structures is about 10 or more. They are usually inclined with respect to the local vertical by about 10–40 degree (Pasachoff, Jacobson, and Sterling 2009). In polar regions, spicules are close to vertical and show a larger extension (BE68). The “traditional” spicules have a lifetime of some 5 to 15 min. In $H\alpha$, they show a velocity of some 25 km s^{-1} and typical chromospheric temperatures of about 10 000 K (Zirker 1962a; Beckers 1972; Matsuno and Hirayama 1988; Makita 2003). At low spatial resolution, they appear to emanate from uni-polar regions (Suematsu, Wang, and Zirin 1995). Finally, it is not clear whether spicules rise smoothly or intermittently.

The spectral signature of spicules varies in the red and blue wings of the $H\alpha$ line. Beckers (1972) noted that this can be due to a variation in Doppler shift or line width (see also Shoji *et al.* 2010). The height and thickness of spicules changes between, e.g., $H\alpha$ and Ca II H \& K . This difference is the joint action of different spatial resolution and smoothing effects at different wavelengths as well as a physical difference in the response of the two lines.

The interest in spicules has revived thanks to new observations with improved spatial resolution, higher temporal cadence or enhanced spectropolarimetric sensitivity. One major source for data of the first two categories is the Solar Optical Telescope (Tsuneta *et al.* 2008) and its instrumentation on-board the Hinode satellite (Kosugi *et al.* 2007). Observations with the 0.3-nm-wide Ca II H interference filter of Hinode have been used to address the structure and evolution of spicules and larger-scale filaments and prominences near the limb (e.g., Suematsu *et al.* 2007; Berger *et al.* 2008), although the two-dimensional (2D) imaging data provides only apparent motions in the sky plane in intensity images. The Hinode Ca filter actually also covers the chromospheric emission of the He I line that contributes up to 30 % to the filter intensity near the solar limb (Beck, Rezaei, and Puschmann 2013). Another source of fast, high-resolution imaging at multiple wavelengths is the Rapid Oscillations in the Solar Atmosphere (ROSA Jess *et al.* 2010) instrument at the Dunn Solar Telescope (DST; Sunspot, USA) which has been used to study, e.g., oscillations inside of spicules (Jess *et al.* 2012).

The information content of high-resolution imaging data was extended to high-resolution imaging spectroscopy with the Interferometric BIDimensional Spectrometer (IBIS; Cavallini 2006; Reardon and Cavallini 2008) at the DST, the GREGOR Fabry-Pérot Interferometer (GFPI; Puschmann *et al.* 2006, 2007, 2012a,b,c, 2013) at the German Vacuum Tower Telescope (VTT; Tenerife, Spain; Schröter, Soltau, and Wiehr 1985), or the CRISP instrument (Scharmer *et al.* 2008) at the Swedish 1-m Solar Telescope (SST; La Palma, Spain). Such data of high spatial resolution in $H\alpha$ and the Ca II IR line at 854 nm have been used to determine the properties of spicules or related features off the limb (Pasachoff, Jacobson, and Sterling 2009; De Pontieu *et al.* 2012) or on the solar disc (Langangen *et al.* 2008; Sánchez-Andrade Nuño *et al.* 2008; Rouppe van der Voort *et al.* 2009; Sekse, Rouppe van der Voort, and De Pontieu 2013).

Data with enhanced polarimetric sensitivity were provided by the Advanced Stokes Polarimeter (ASP; Skumanich *et al.* 1997) at the DST in the He I D_3 line (e.g., Casini *et al.* 2003; López Ariste and Casini 2005), the Tenerife Infrared Polarimeter (TIP; Martínez Pillet *et al.* 1999; Collados *et al.* 2007) at the VTT in the He I line at 1083 nm (e.g., Centeno, Trujillo Bueno, and Asensio Ramos 2010; Martínez González *et al.* 2012), the SPINOR instrument (Socas-Navarro *et al.* 2006) at the DST in He I at 1083 nm and the Ca II IR lines (Socas-Navarro and Elmore 2005), the polarimetric mode of the THEMIS telescope (López Ariste, Rayrole, and Semel 2000; Paletou *et al.* 2001), or the Zürich Imaging Polarimeter (ZIMPOL; Gandorfer *et al.* 2004) at the Gregory-Coudé Telescope in Locarno in the He I D_3 line (e.g., Ramelli *et al.* 2006).

The new data allowed old observational and theoretical results on spicules to be revised. With the spectropolarimetric observations, the magnetic field

strength in spicules could be determined to be between 10 G and 50 G (Trujillo Bueno *et al.* 2005; Centeno, Trujillo Bueno, and Asensio Ramos 2010). Orozco Suárez, Asensio Ramos, and Trujillo Bueno (2015) found a decrease in magnetic field strength from 80 G at the limb to 30 G at a height of 3 Mm above it. De Pontieu *et al.* (2007a) introduced two types of spicules based on their lifetime (15 min for type I vs. 2 min or less for type II; see also Rouppe van der Voort *et al.* 2009), where short-lived spicules are also generally thinner and show faster apparent velocities than traditional spicules, although already BE68 described two types of spicules differing in their line widths. De Pontieu *et al.* (2007a) stated that most of the type II spicules do not show a descent, but fade from sight *in situ*, which could be caused by a rapid heating to transition-region and coronal temperatures. It is not clear at present whether these new and old two types correspond eventually to the same classification and what the exact differences between type I and type II spicules are. Avery (1970) explained the two types of spicules defined by BE68 as being solely caused by different (or absent) rotation. Pereira, De Pontieu, and Carlsson (2012) suggested that the two types of spicules of BE68 would fall into the new type I category as defined by De Pontieu *et al.* (2007a), whereas the new type II spicules should have been undetectable at the temporal and spatial resolution of older observations (cf. also Pereira, De Pontieu, and Carlsson 2013). Zhang *et al.* (2012) re-analyzed the data used by De Pontieu *et al.* (2007a) and found both an ascending and descending phase for most of their spicule examples. They questioned the existence of type II spicules as being somehow different from the classical type I spicules (see also the discussion in Skogsrud *et al.* 2015).

There are suggestions that different mechanisms work on different type of spicules (Hammer *et al.* 2008; Martínez-Sykora *et al.* 2009) and various theoretical models have been proposed (Sterling 2000, and references therein). Such models have to provide a source of energy to support spicules against gravity, to accelerate them upwards, and to explain their elongated shape and temporal evolution. Candidates for the energy source are photospheric impulsive events (Hollweg 1982; Suematsu *et al.* 1982; De Pontieu, Erdélyi, and James 2004) and energy sources that are related to magnetic fields, such as Alfvén waves (e.g., De Pontieu and Haerendel 1998; Kudoh and Shibata 1999; Hansteen *et al.* 2006; Rouppe van der Voort *et al.* 2007), small-scale reconnection events (Hegglund, De Pontieu, and Hansteen 2009; Yurchyshyn, Abramenko, and Goode 2013) or localized currents that accelerate material by the Lorentz force (Martínez-Sykora, Hansteen, and Moreno-Insertis 2011; Goodman 2012). There are indications that the height extension of spicules is affected by the transition-region height and vice versa (Shibata and Suematsu 1982; Guerreiro, Carlsson, and Hansteen 2013). Magneto-hydrodynamical (MHD) wave models of spicules (Kulidzanishvili and Zhugzhda 1983; Kukhianidze, Zaqarashvili, and Khutsishvili 2006; He *et al.* 2009) are motivated by observations of oscillations and observed Doppler shifts (the so-called line tilt) that again date back to BE68 and before. Despite a lot of observational constraints, no canonical model for spicules that matches their principal observed dynamical properties could be derived.

Because spicules, or more precisely, type II spicules according to the new definition, were found to be abundantly present on the solar surface, they potentially could transport a significant amount of energy into the corona (De Pontieu

et al. 2009). As discussed by Judge *et al.* (2012), this idea of a coronal energy input from the chromosphere was suggested already earlier on (Athay and Holzer 1982; Athay 2000), but there were only indirect proofs for this process, e.g., the amount and direction of (vertical) net mass flows (Pneuman and Kopp 1978). Most of the argumentation for a relation between the chromospheric spicules and the transition region or corona was based on the dynamic evolution and the dynamic properties of spicules (LOS velocities, acceleration/deceleration on disc centre and near the limb; e.g., McIntosh and De Pontieu 2009). Madjarska, Vanninathan, and Doyle (2011) were unable to find coronal counterparts to three large-scale macrospicules (cf. Bohlin *et al.* 1975; Pike and Harrison 1997; Kamio *et al.* 2010; Scullion, Doyle, and Erdélyi 2010; Murawski, Srivastava, and Zaqarashvili 2011) seen in Ca II H imaging from Hinode. Pereira *et al.* (2014) and Rouppe van der Voort *et al.* (2015) found counterparts to spicules in transition-region lines at the limb and on the disc, respectively.

Here, we investigate a possible connection of spicular material to atmospheric layers above the chromosphere by determining the maximal height above the solar limb attained by different kinds of features and by deriving the height dependence of the line width in various chromospheric spectral lines. Assuming a heating process from chromospheric (5000 to 20,000 K) to transition-region temperatures ($> 10^5$ K) during their rise, the line width in resolved spectra should increase with height if the upper end of spicules gets heated.

Section 2 describes the various data sets covering several chromospheric spectral lines (Ca II H, H ϵ , H α , Ca II IR at 854.2 nm, He I at 1083 nm) in one-dimensional (1D) and two-dimensional (2D) spectroscopy. The data reduction and the quantities derived from the spectra are explained in Sect. 3. The results of Sect. 4 are summarized in Sect. 5 and discussed in Sect. 6. Section 7 provides our conclusions. Appendix A shows a few more examples of time-series of imaging spectroscopy in H α . Appendix B discusses the significance limits of the profiles and the analysis approach while Appendix C shows additional examples of spectrograph observations.

2. Observations

For the simultaneous observations of up to five chromospheric spectral lines in four different wavelength regimes from the near-ultraviolet (UV) to the near-infrared (IR), we used different combinations of the post-focus instruments available at the VTT at that time: the main Echelle spectrograph for spectropolarimetric observations of He I 1083 nm with TIP and simultaneous spectroscopy of Ca II IR at 854.2 nm with a PCO 4000 camera; the Triple Etalon Solar Spectrometer (TESOS; Kentischer *et al.* 1998; Tritschler *et al.* 2002) for imaging spectroscopy of H α ; the POLarimetric LIttrow Spectrograph (POLIS; Beck *et al.* 2005) for spectroscopic observations of Ca II H, H ϵ and H α . The two combinations of the instruments that we used are described in detail in Beck and Rezaei (2012). Their main difference is the usage of TESOS for 2D spectroscopy in H α in 2010 (setup 1), while in 2011 all lines were observed with slit-spectrographs (setup 2). Table 2 lists the spectral and spatial characteristics of the data that only vary for Ca II H and H α .

Table 1. Spatial and spectral characteristics of the data.

line	dispersion pm/pixel	wavelength nm	slit width "	spat. sampl. "/pixel
Setup 1 & 2: TIP & Echelle spectrograph				
He I	1.1	1082.34–1083.45	0.36	0.18
Ca II IR	0.82	853.45–855.10	0.36	0.18
Setup 1: TESOS and POLIS				
H α ¹	4.9	656.16–656.39	–	0.09
Ca II H ²	1.45	395.86–398.75	0.5	0.22
Setup 2: POLIS				
H α ²	2	654.22–657.61	0.5	0.22
Ca II H ³	1.92	396.34–396.95	0.5	0.292
Setup 3: GFPI				
H α	11.1	656.17–656.40	–	0.11

¹: TESOS ²: PCO 4000 in POLIS ³: default POLIS CCD

In setup 1, TESOS was run without direct synchronization to the scanning. We set it to a continuous observing mode as soon as the adaptive optics (AO) was locked near the limb. The cadence of TESOS was either about 20 or 30 s, depending on whether a second line (Mg I at 517 nm) was recorded in addition to H α . The TESOS field of view (FOV) was circular with a diameter of 40". In both setups, we aimed for observations of spicules in three different observing modes of the spectrograph instruments: large-area maps, time-series (ts), and long-integrated (> 30 s) small-area maps. All three types of observations were done with the slit parallel and perpendicular to the limb. The fastest cadence in the slit-spectrograph data was 80 seconds and the integration time per scan step, t , varied between 6 seconds and 2 minutes.

We finally selected only a subset of five specific observations for the current study. The corresponding settings are listed in Table 2. In all observations, the chromospheric spectral lines of He I at 1083 nm, Ca II IR at 854.2 nm, H α at 656 nm and Ca II H at 396.85 nm were observed simultaneously. In setup 1 (observations Nos. 1 to 4), also He I at 397 nm was covered in the POLIS data and the H α line was recorded with a 2D spectrometer, but only sampled within a limited spectral range. In setup 2 (observation No. 5), the spectral range around H α was extended because of observing it with a slit-spectrograph, but He I was not covered anymore in the Ca II H spectra because of using the default Ca CCD of POLIS.

In addition to the multi-line observations described above, we used a time-series of about 15 min obtained with the GFPI on 04/05/2005 at the VTT (setup 3) in only the H α line. The spectral line was sampled in 21 steps of 11 pm width with a cadence of about 22 s (Puschmann *et al.* 2006). The spectra were reconstructed with the Multi-Object Multi-Frame Blind Deconvolution

Table 2. Settings of the observations.

No.	1	2	3	4	5
date	30/06/2010	01/07/2010	01/07/2010	02/07/2010	12/04/2011
time [UT]	07:48–08:08	07:56–08:24	08:59–09:19	08:11–08:24	07:50–08:14
pos. x''/y''	–864/349	–868/293	–868/293	–354/–836	–933/172
type	QS/map	QS/map	QS/map	QS/ts	AR/map
t [s]	10	60	6	6	8
steps ¹	100×0.3	25×0.3	150×0.3	20×0.5×5	150×0.36
duration [min]	20	28	19	13	25
cadence [s]	30 ²	20 ²	20 ²	156 ³	–
angle ⁴ [deg]	90	90	90	0	90
setup ⁵	1	1	1	1	2
No.	6				
date	04/05/2005				
time [UT]	08:47–09:02				
pos. x''/y''	south pole				
type	QS/ts				
t [ms]	20				
steps	39				
duration [min]	15				
cadence [s]	~ 20				
setup ⁵	3				

¹: number of steps × step width in arc-seconds (× number of repetitions of the scan) ²: cadence of TESOS spectra ³: cadence of slit-spectrograph spectra ⁴: angle relative to the solar limb ⁵: setup 1: TIP, TESOS and POLIS; setup 2: TIP and POLIS; setup 3: GFPI

Technique (MOMFBD; Löfdahl 2002; van Noort, Rouppe van der Voort, and Löfdahl 2005) as part of the Imaging Spectropolarimetric Parallel-Organized Reconstruction Data Pipeline (ISPOR-DP), the GFPI data pipeline described in Puschmann and Beck (2011). These data have the highest spatial resolution within our sample. The spectra covered a similar wavelength range as the H α spectra from TESOS but had a coarser spectral sampling.

Figure 1 shows the locations of the FOVs of the observations overlaid on cut-outs from LOS magnetograms from MDI (observations No. 1, 2/3, 4 and 6) and HMI (No. 5) and from GONG H α images (all but No. 6), respectively. All data apart from observation No. 5 were taken in areas of quiet Sun (QS), while No. 5 was taken in active region (AR) NOAA 11191. There are no discernible large-scale structures such as prominences in the H α images that could have had an impact on the observations close to the limb. All observations benefited from the real-time correction of wavefront deformations by the Kiepenheuer-Institut AO system (KAOS; von der Lühe *et al.* 2003). Apart from the observations in 2011, where a sunspot was located close to the limb, a facula was selected as AO lock point. The latter was possible because at the VTT the light level in the

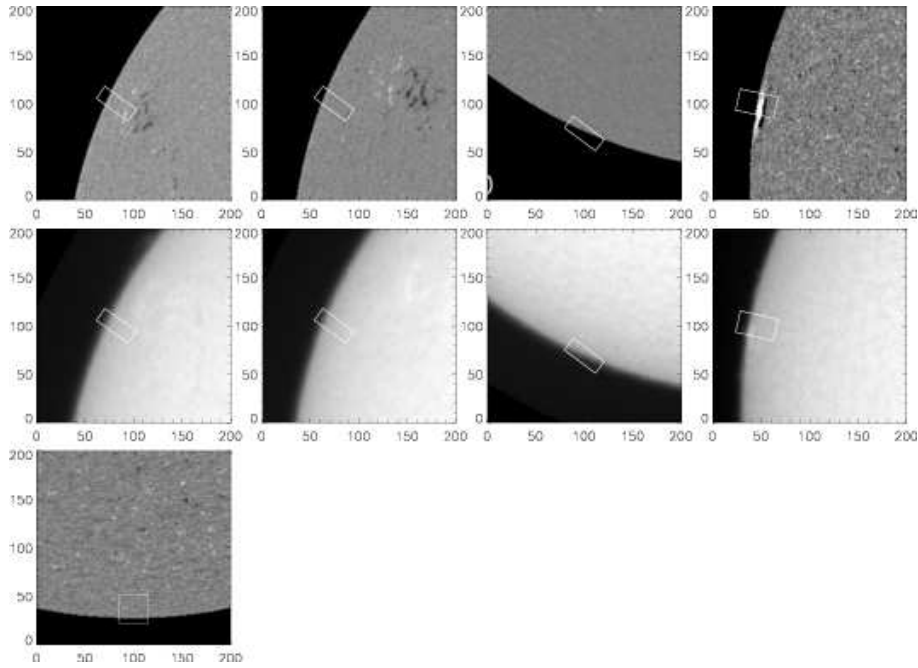


Figure 1. Location of the FOVs on full-disk LOS magnetograms and $H\alpha$ images. Top row (2nd row), left to right: observations No. 1, 2/3, 4 and 5 overlaid on a magnetogram ($H\alpha$ image). Bottom row: observation No. 6 overlaid on a magnetogram. Tick marks are in arcsecs.

AO wave front sensor could be adjusted by a motorized grey wedge and the AO software removed intensity gradients before the correlation of sub-apertures.

3. Data reduction and analysis

We corrected the spectra from all instruments for the dark current of the CCDs. The removal of flat-field defects had to be adjusted for each spectral line and instrument. In this section, we describe the additional data reduction steps or analysis methods that are particular for the off-limb data.

3.1. Stray-light correction

For observations on the solar disc, stray light contaminates the data with about 20 % of spurious light (e.g., Beck, Rezaei, and Fabbian 2011; Beck *et al.* 2013). For off-limb regions, the intrinsic intensities are rapidly dropping to below 20 % of the disc-centre values (e.g., Beck and Rezaei 2011) and thus stray light becomes critical. There are some observational approaches to minimize stray light in off-limb observations, such as putting the spectrograph slit parallel to the limb (Centeno, Trujillo Bueno, and Asensio Ramos 2010) or blocking the part of the slit (or FOV in general) that remains on the disc with an opaque cover similar to a coronagraph (Socas-Navarro and Elmore 2005). However, some contamination of off-limb observations with light from the disc can still not be avoided.

To reduce the stray-light contamination of the data, we used two different methods. The first was based on the – theoretically correct – approach of modeling the off-limb stray light from the intensities observed on the disc (Zwaan 1965; Staveland 1970; Mattig 1983; Martinez Pillet 1992; Beck, Rezaei, and Fabbian 2011). A spatially- and/or temporally-averaged line profile was calculated for the on-disc region of the FOV that was furthest from the limb (about $10''$ - $30''$) in each data set. Using the observed intensities on cuts across the limb, or a theoretical modeling or measurement of the spatial point-spread function (PSF), a suited stray-light fraction as a function of the limb distance can be determined (cf. Beck, Rezaei, and Fabbian 2011; Löfdahl and Scharmer 2012). The fraction is multiplied with the average on-disc profile and subtracted from the observed spectra. This method has the drawback that the region of the FOV that is still on the disc might actually not cover the full area from which the stray light originated from, e.g., the FOV would always need to cover the full solar disc in theory. This method thus commonly leaves some residuals far away from the limb because the average profile used is not identical to the real stray-light profile, but it provides a smooth stray-light correction across the limb without any discontinuities or intensity jumps at the limb location.

There exists a second, more empirical approach for off-limb stray-light correction. The stray-light profile to be subtracted is determined from some off-limb region that is far away from the limb and from any true solar feature (e.g., Sánchez-Andrade Nuño *et al.* 2007; Martínez González *et al.* 2012). With this approach, one uses the result of the stray-light contamination instead of the theoretical source of the stray light. The fraction of the stray-light profile to be subtracted can then be determined from the residual intensity at continuum wavelengths divided by the corresponding intensity in the stray-light profile. The advantage of this method is a good stray-light correction far away from the limb, but it usually shows a worse correction close to the limb. It also creates a discontinuity in intensities at the location of the limb itself, which also has to be defined by some ad-hoc criterion. Because we are mainly interested in the properties of off-limb spectra, we used the second method for most data sets, apart from those where a stray-light correction based on the first method already had been applied to the data for previous studies. No stray-light correction was applied to the reconstructed GFPI spectra that showed little stray light after the deconvolution.

3.2. Determination of line parameters

Most of the data are either spatially or spectrally over-sampled. To increase the signal-to-noise ratio, we thus binned most of the spectra by two in the spatial and/or spectral dimension before deriving the line properties in individual profiles.

For all observations and all wavelength ranges, we used the average line profile from the on-disc region of the FOV that was furthest from the limb to determine an intensity normalization coefficient and any other needed corrections, e.g., linear or low-order intensity trends in the dispersion direction, that matched the average observed spectra to the corresponding Fourier transform spectrometer

(FTS; Kurucz *et al.* 1984; Neckel 1999) solar atlas profiles. All other spectra of a given data set were then normalized and/or corrected with these values. For all on-disc and off-limb spectra, we derived the continuum intensity I_c from some continuum wavelength range and a generic line-core intensity I_{core} from an integration over the line-core region in the spectra. The maps of I_c were used to co-align the observations in different wavelengths that showed offsets by differential refraction (e.g., Appendix A of Beck *et al.* 2008; Felipe *et al.* 2010).

To determine the line width in individual spectra, we fitted single Gaussians to the line profiles. The central self-absorption in the line profiles disappears for heights larger than about 3 Mm above the limb, leaving a roughly Gaussian shape (see Figs. 18 and 19 below). The spectral range to be analyzed was restricted each time to cover only the respective emission profile of a single line for the fit. The Ca II H spectra recorded with a PCO were the only case where two separate fits were performed to a single profile, i.e., one for Ca II H and one for H ϵ . The Gaussian fit yielded the central amplitude, the central position and the full-width at half-maximum (FWHM) of the Gaussian. The position of the Gaussian was converted to the corresponding LOS velocity using the line-core position in the average profiles as zero-point reference.

As a cross-check of the width derived by the Gaussian fit, we also used a simpler method that only determined the maximal intensity of the emission profile and the two positions where the intensity dropped to half of it. The FWHM is then directly given by the distance between these two positions.

The fit of a Gaussian function to the GFPI spectra worked less reliably because the outermost wavelength points in the blue and red wings often still sample the line emission without a clear drop of intensities, which also made the determination of the FWHM with the direct method impossible. The line parameters for the GFPI spectra are thus not as well defined as for the other data.

3.3. Derivation of kinetic temperature and non-thermal line width

The line width $\Delta\lambda$ of emission lines formed in the optically-thin regime can be described by

$$\Delta\lambda = \frac{\lambda}{c} \sqrt{\frac{2RT_{\text{kin}}}{\mu} + v_{\text{non-th}}^2}, \quad (1)$$

where λ is the central wavelength, c the speed of light, R the universal gas constant, T_{kin} the kinetic temperature, μ the molecular weight and $v_{\text{non-th}}$ any additional non-thermal line broadening (e.g., Tandberg-Hanssen 1960; Bendlin, Wiehr, and Stellmacher 1988). Magnetic broadening also contributes to the line width, but for typical chromospheric field strengths below 100 G (e.g., Centeno, Trujillo Bueno, and Asensio Ramos 2010) it presumably is negligible in spicules and prominences.

The line width $\Delta\lambda$ is related to the FWHM in the case of a Gaussian emission profile by

$$\Delta\lambda = \frac{\text{FWHM}}{2\sqrt{\ln 2}} = \sqrt{2}\sigma, \quad (2)$$

where σ is the width of the Gaussian¹.

With line widths of two simultaneously observed spectral lines from two different chemical elements with different molecular weights μ_i , one can derive an estimate for both the kinetic temperature and the velocity equivalent of the non-thermal line broadening. For $n > 2$ observed spectral lines, Eq. 1 leads to a set of n equations for the two open parameters T_{kin} and $v_{\text{non-th}}$ that can be solved by a matrix inversion or a least-square fit.

The whole approach assumes emission profiles of Gaussian shape, i.e., without central reversals by self-absorption, and that the observed spectral lines have to form in the same solar atmospheric volume or at least under the same atmospheric conditions. With the variation of opacity from line to line in the chromosphere, the second condition needs not be fulfilled automatically even for features that appear to be on the same spatial location in the data (e.g., Stellmacher and Wiehr 2015). The first condition can be estimated from the line shape.

We determined T_{kin} and $v_{\text{non-th}}$ using Eqs. 1 and 2 for all pairs of lines and all lines together only for the data taken in 2011 because they could be aligned precisely thanks to their high spatial resolution. The width σ of the Gaussians that were fitted to the profiles was corrected beforehand for the instrumental broadening σ_{instr} of the respective spectrograph (Tandberg-Hanssen 1960, his Eq. II.12). The value of σ_{instr} was determined by convolving the FTS atlas profiles with a Gaussian to match the line width of photospheric lines in the observed spectra (cf. Cabrera Solana *et al.* 2007). The velocity equivalents of the instrumental broadenings were, however, only about 2 km s^{-1} , which turned out to be nearly negligible in comparison to $v_{\text{non-th}}$. Therefore, this correction had only a small impact on the final values of T_{kin} and $v_{\text{non-th}}$.

4. Results

4.1. 2D spectroscopy in H α

4.1.1. GFPI data

Figure 2 shows one of the 39 scans through the H α line taken with the GFPI (observation No. 6, setup 3). An animation of the complete time-series is available in the online section (see also Puschmann 2016). Individual spicules can best be identified in the line-wing image, while in the line-core image the complete off-limb region shows a more diffuse emission pattern. In the maps of the FWHM from the Gaussian fit (top right panel of Fig. 2), individual spicules show an increased FWHM relative to their surroundings, but in most cases without any clear trend along their length.

¹We note that in some older literature, the use of $\Delta\lambda$ in this context varies, sometimes standing for the half-width at half-maximum (i. e., $\Delta\lambda = \frac{\text{FWHM}}{2}$), while in yet other instances the term “half-width” is used for the FWHM or an exponential of the form $\exp^{-(x/\sigma)^2}$ is used.

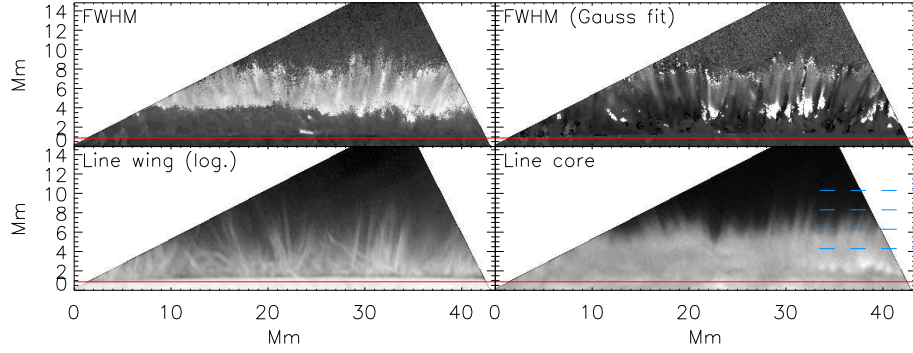


Figure 2. Example of the GFPI $H\alpha$ observations at the limb (observation No. 6). Bottom row, left to right: line-wing intensity in logarithmic display and line-core intensity. Top row, left to right: FWHM from direct determination and FWHM from fit of a Gaussian. The red horizontal line marks the approximate location of the limb. The blue dashed lines in the lower-right panel indicate the heights above the limb of the spectra shown in Fig. 5. An animation of the complete time-series is available in the online section.

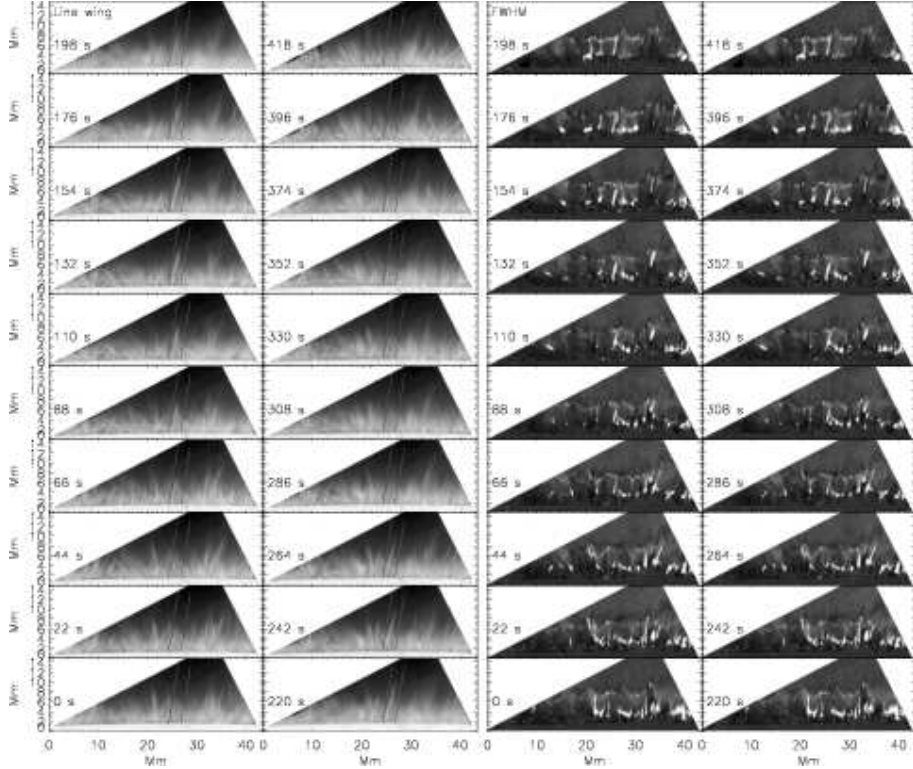


Figure 3. Evolution of an individual spicule in line-wing images (left panels) and in maps of the FWHM from a Gaussian fit (right panels) in the GFPI $H\alpha$ data. The spicule is located between the two inclined red lines in each sub-panel. It starts at about $t = 44$ s and has disappeared at $t = 396$ s. See also the animation of the complete time-series in the online section.

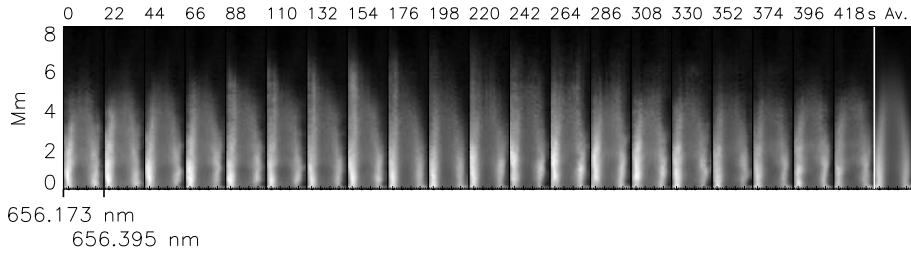


Figure 4. Individual spectra during the evolution of the spicule indicated in Fig. 3. The wavelength increases from left to right in each sub-panel, within the range marked for the leftmost sub-panel. The rightmost panel shows the off-limb spectra in the GPFI data averaged over all 39 bursts and all spatial positions along the limb.

To trace the temporal evolution of the emission, we selected one prominent spicule within the time-series (Figs. 3 and 4). It can be clearly distinguished in the line-wing images at $t = 44$ s (left column in Fig. 3, third panel from the bottom) and can be followed until $t = 396$ s. Its line width is larger than that of the surroundings (Fig. 3, third and fourth column), but reduces with increasing limb distance in most cases. The spectra along the central axis of the spicule (Fig. 4) resemble those from the TESOS data in Fig. 7, but show larger Doppler shifts, especially towards the blue at the beginning ($t = 88 - 220$ s). The spicule expands up to a height of about 6 Mm at $t = 242$ s. The average spectra from all spatial locations and all of the 39 wavelength scans show a reduction of the line width with increasing limb distance (rightmost panel in Fig. 4).

Because of the difficulties in extracting the line width from the GPFI spectra, we also selected individual spectra at different heights above the limb to follow their temporal evolution (Fig. 5 and the animation in the online section). Figure 5 shows the temporal evolution of individual spectra at four of those heights above the limb. Like in the animation, the presence of large and varying Doppler shifts is clearly visible, but the disappearance of some bright emission is usually not connected to an increase in line width but only to a fading with time.

4.1.2. TESOS data

Figure 6 shows line-core images in $H\alpha$ taken with TESOS during observation No. 1 (cf. Table 2, setup 1). The cadence between subsequent images is about 30 seconds. The corresponding FOV in the other spectral lines is shown in Fig. 10 below. In the top left panel of Fig. 6, the approximate location of the TIP slit inside the TESOS-FOV is indicated by a dash-dotted horizontal line. Each line-core image is displayed twice: with and without an unsharp masking that enhances small-scale features. The limb location was determined from the corresponding continuum intensity images (not shown) and was used to delineate the region in which the stray-light correction with the second correction method (Sect. 3.1) was applied. Its approximate location shows up at about the middle of the FOV as a vertical line in each image. The FOV is slowly drifting with time because of the co-temporal scanning of the slit-spectrograph instruments. To extract the spectral properties of individual spicules, we masked some intensity

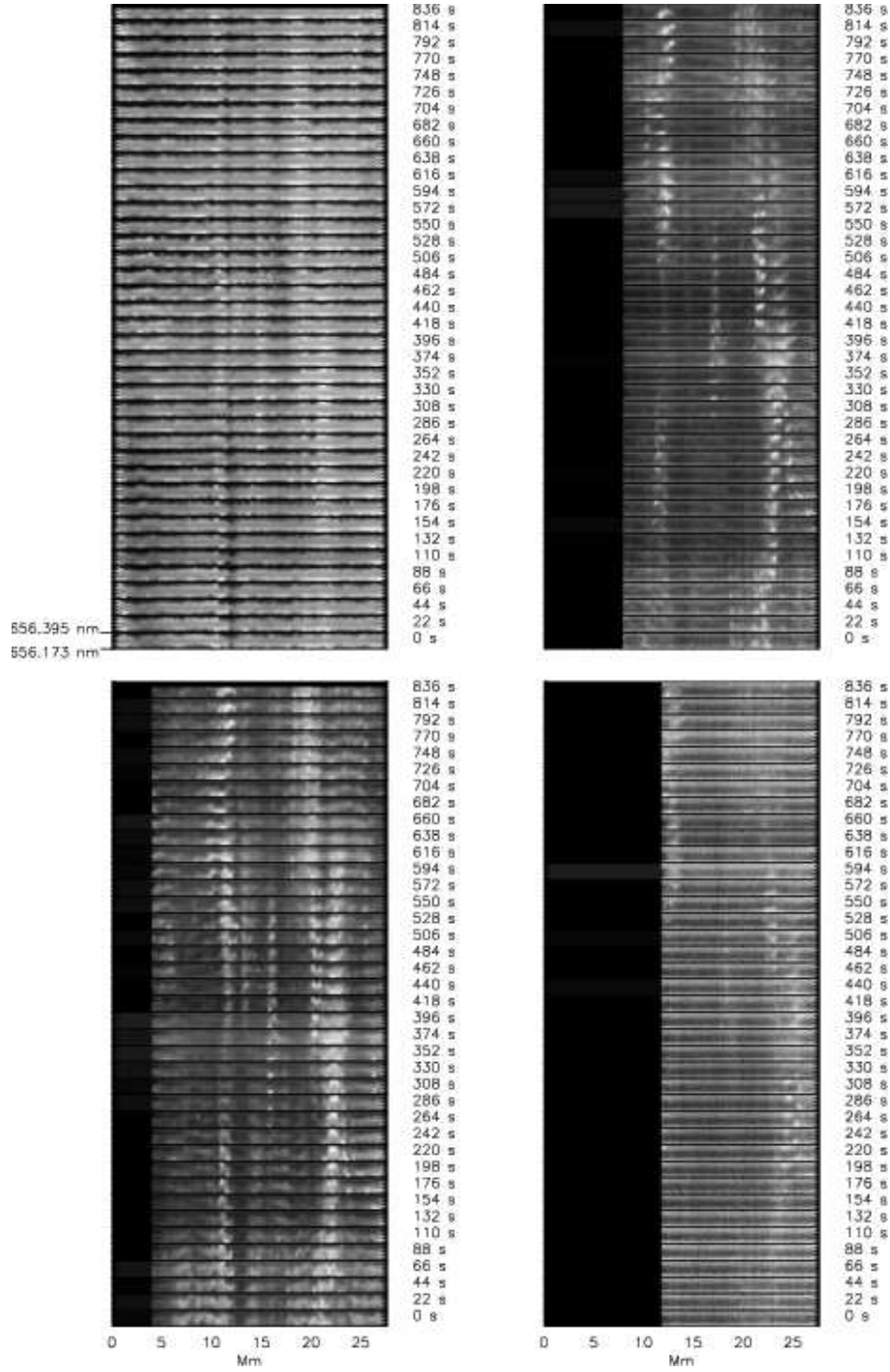


Figure 5. Temporal evolution of $H\alpha$ spectra at different heights above the limb in the GFPI data. Left column: $h = 4.3$ Mm (top), $h = 6.3$ Mm (bottom). Right column: $h = 8.3$ Mm (top), $h = 10.3$ Mm (bottom). Time increases from bottom to top and the spatial position along the limb increases from left to right in each panel. The wavelength increases from bottom to top in each sub-panel, within the range marked in the lower sub-panel of the top-left panel. See also the animation of the complete time-series in the online section.

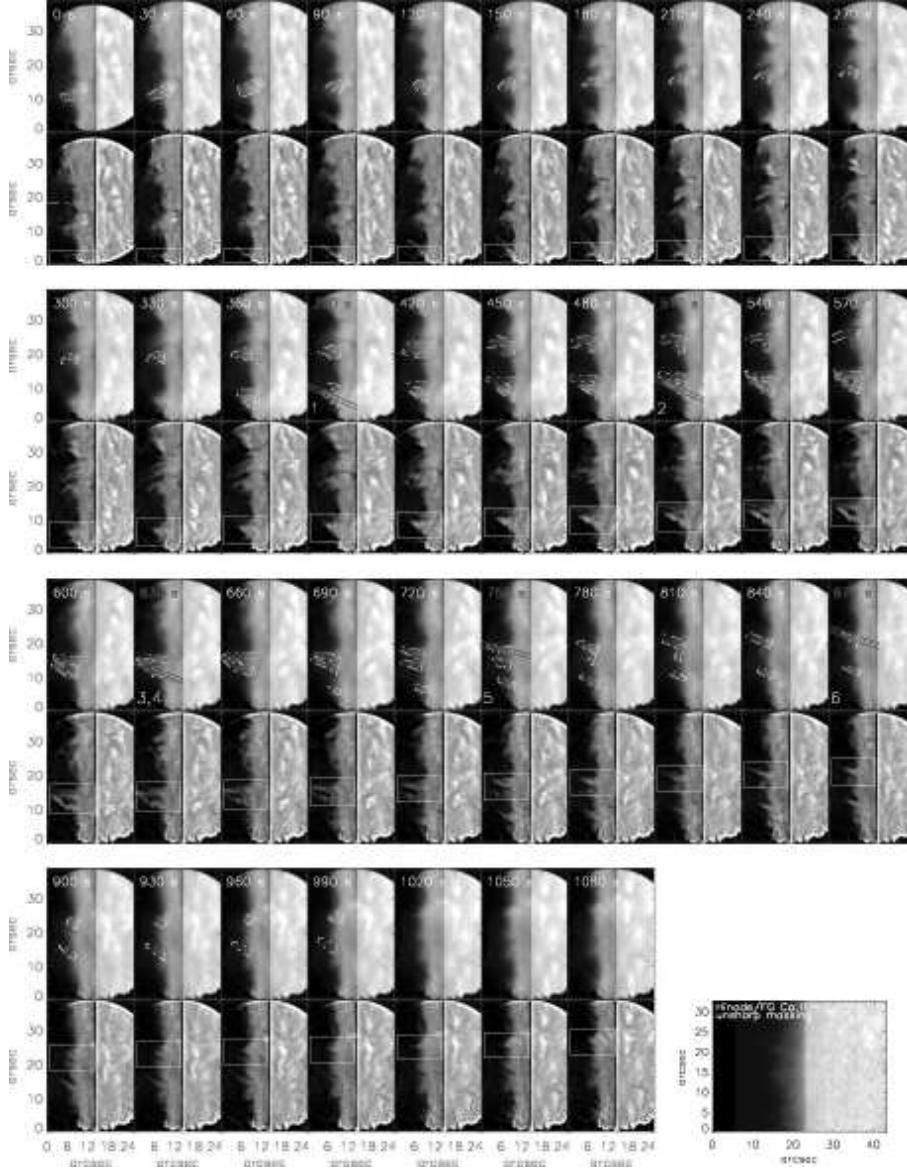


Figure 6. $H\alpha$ line-core images acquired with TESOS during observation No. 1. Time increases from left to right and top to bottom. For each time step, the original (unsharp-masked) line-core image is displayed in the upper (lower) panel. The white dash-dotted contour lines mark the area of some individual spicules. The white rectangles follow the location of one specific feature with time. The red- and blue-hatched areas (with corresponding time of observation given in red in the relevant sub-panels) denote the range of averaging for the profiles 1 to 6 shown in Fig. 7. The orange dash-dotted line at $t = 0$ s indicates the location of the TIP slit. The bottom rightmost panel shows a cut-out from a broad-band Ca II H image from Hinode for comparison.

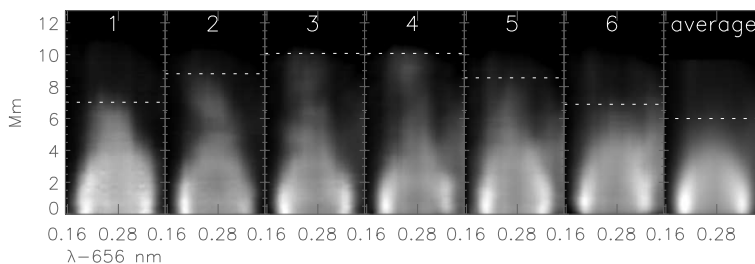


Figure 7. Average $H\alpha$ profiles in one spicule feature. Left to right/1–6: red hatched area of Fig. 6 at $t = 390, 510, 630$ s, blue hatched area at $t = 630$ s, red hatched area at 750 and 870 s. The rightmost panel shows the average off-limb profiles. The horizontal white dotted lines denote the maximal height where the spectra are still significant.

enhancements in the $H\alpha$ line core above a height of about 5 Mm beyond the limb (white dash-dotted contours in the top panels of a given row). We note that below this height it is nearly impossible to reliably identify individual features in line-core images because of the complete overlap of different features.

We selected one feature that was covered during all of its life-time (cf. the white rectangles in Fig. 6) to determine laterally averaged profiles along its extent at five different time steps (cf. the six blue and red-hatched areas marked in Figure 6). The feature, or at least a predecessor of the feature at the same spatial location, can be identified already at $t = 60$ s (third column in top row; $x, y \sim 8'', 3''$) if one follows its evolution backwards in time. It rises over the course of ~ 300 s to a maximal height of about $16''$ above the limb at $t = 630$ s. It retracts subsequently towards the limb and cannot be identified anymore at $t = 930$ s.

Figure 7 shows the spatially-averaged line profiles, i. e., those obtained averaging laterally along the y -axis of the images in Fig. 6 over the colored hatched areas (labeled 1 to 6 in Figure 7) at the corresponding time step during the observations, with limb distance increasing along the vertical direction in the figure. The feature is roughly oriented (tilt of less than 30 degrees) perpendicular to the limb, so the laterally averaged profiles roughly sample its extent in height above the limb. The temporal variation of its maximal height (marked as a horizontal white dotted line in each panel of Fig. 7) is roughly parabolic. The profiles all show a change from self-absorption with a central absorption core up to a height of about 2 Mm above the limb to pure emission profiles at higher layers. In the visual impression, the line width is constantly reducing with height. The same holds for the average off-limb profiles shown in the rightmost panel of Fig. 7 that were retrieved by averaging over nearly the full extent of the FOV, excluding the top and bottom borders because of the curved field stop. In the profiles averaged over the full usable FOV, only spectra up to about 6 Mm above the limb have intensities higher than the noise level, similar to the GFPI spectra in Fig. 4. The profiles marked as 4 to 6 in Figure 7 exhibit a faint haze at the red end of the spectrum ($\lambda \sim 656.34$ nm) which is some flat-field residual that could not be corrected for.

The individual profiles along the two branches of the feature that have developed at $t = 630$ s (marked as red and blue-hatched areas in the corresponding

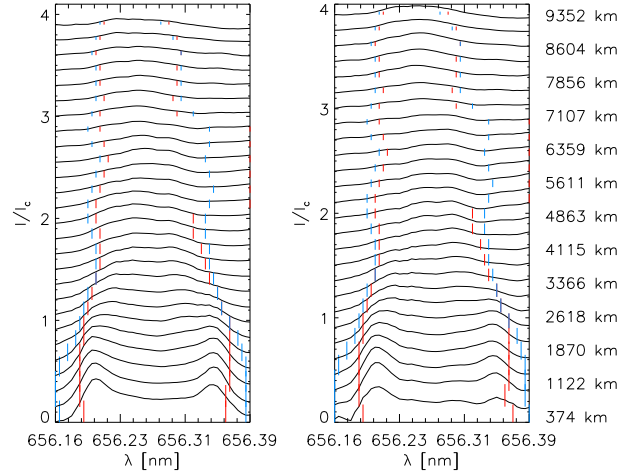


Figure 8. Individual profiles from the laterally averaged sets of spectra Nos. 3 (left) and 4 (right) of Fig. 7. The profiles are displaced from each other in y for better visibility. The corresponding heights above the limb are given at the right-hand side. The blue/red bars denote the FWHM from a Gaussian fit and the locations where the intensity drops to 50 % of its maximum, respectively.

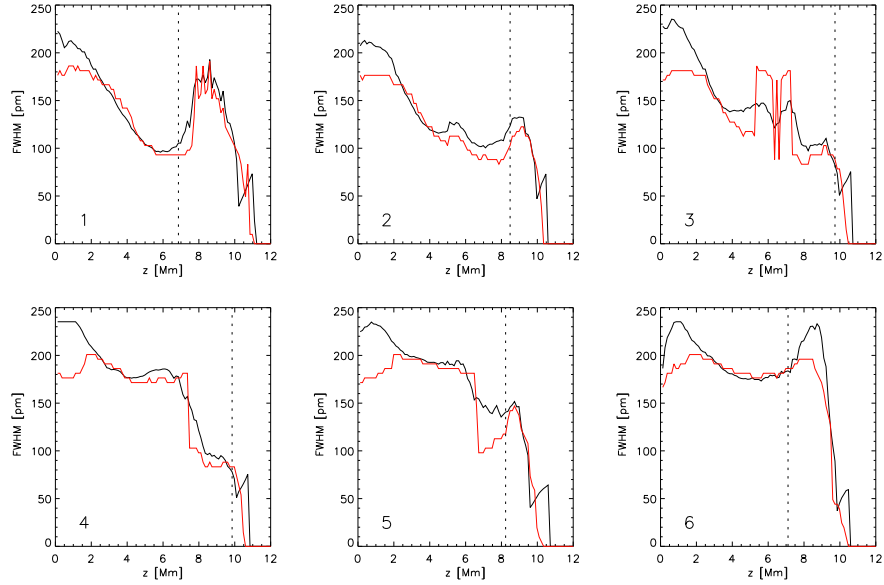


Figure 9. The FWHM of the same $H\alpha$ profiles of Fig. 7. Black: FWHM from the Gaussian fit. Red: FWHM from the locations where the intensity drops to 50 % of the maximum. The vertical dotted lines denote the maximal height where the spectra are still significant.

panel of Fig. 6) are shown in Fig. 8. The FWHM derived from the Gaussian fit and that derived directly are over-plotted with short red and blue coloured bars, respectively. The FWHM is seen to reduce up to a height of about 5 Mm above the limb, and remains at best constant at higher layers. The corresponding FWHMs in all six sets of laterally averaged profiles are shown in Fig. 9. Up to the height where the intensity in the spectra is still significant, all six examples of the height variation in the FWHM in resolved features show a monotonic decrease in width. The FWHM only increases just where the spectra level off into the noise (profile sets 1, 2 and 6 in Fig. 9). The FWHM retrieved via Gaussian fitting agrees reasonably well for most spectra with that obtained using the direct method, which, however, seemingly tends to give noisier results. This might be related to the fact that the Gaussian fit makes use of all wavelength points in the line profile, whereas the direct method is based on three wavelength points only, i.e., the one corresponding to maximum intensity and the two locations for which the line profile reaches a level of 50 % of that value. The latter method is therefore more sensitive to noise peaks.

Other examples of time-series of $H\alpha$ line-core images are shown in Figs. 21 to 24 in Appendix A. They all share more prominently than Fig. 6 a certain peculiarity, which, however, is also apparent in the latter: the majority of the individual structures or features that are seen above a limiting height of about 5 to 6 Mm show little to no resemblance to spicules, i.e., only a very few features are elongated, slender brightenings jutting out and away from the limb. Figures 21 and 22 clearly show material, or more precisely, brightenings that recede from the limb upwards (bottom rows of both figures), but the corresponding shapes are either elongated structures that are parallel to the limb, or roundish blobs. The same holds for Fig. 23: only complex-shaped features appear at heights of more than about 6 Mm above the limb in the $H\alpha$ line-core images.

4.2. (Pseudo-)slit-spectrograph data

The left four panels of Fig. 10 show the corresponding FOV of observation No. 1 in the slit-spectrograph data. We constructed a pseudo-scan map (e.g., Beck *et al.* 2007) of the same FOV from the 2D $H\alpha$ spectra from TESOS. We selected the TESOS wavelength scan closest in time to each scan step of the slit-spectrograph instruments for that purpose and cut out the corresponding spectra along the location of the TIP slit from the TESOS 2D FOV (top left panel of Fig. 6). The resulting map (upper left subpanel of Fig. 10) shows how the temporal evolution of Fig. 6 is sampled in a slit-spectrograph observation. A prominent change is that most laterally extended structures in the 2D $H\alpha$ line-core images appear as a series of resolved, rather thin and elongated features in the pseudo-scan map. We did not try to improve the spatial alignment because due to the large differential refraction at the early time of this observation and the sequential scanning, all other spectra in the different wavelength ranges are not strictly co-spatial and simultaneous anyway.

The line-core images in $H\alpha$, $Ca II H$ and $He I$ at 1083 nm are to some extent similar, showing one set of spicular features at $x \sim 5$ Mm, a region of reduced extent of emission from $x = 7$ to 12 Mm, and a double pair of spicules at

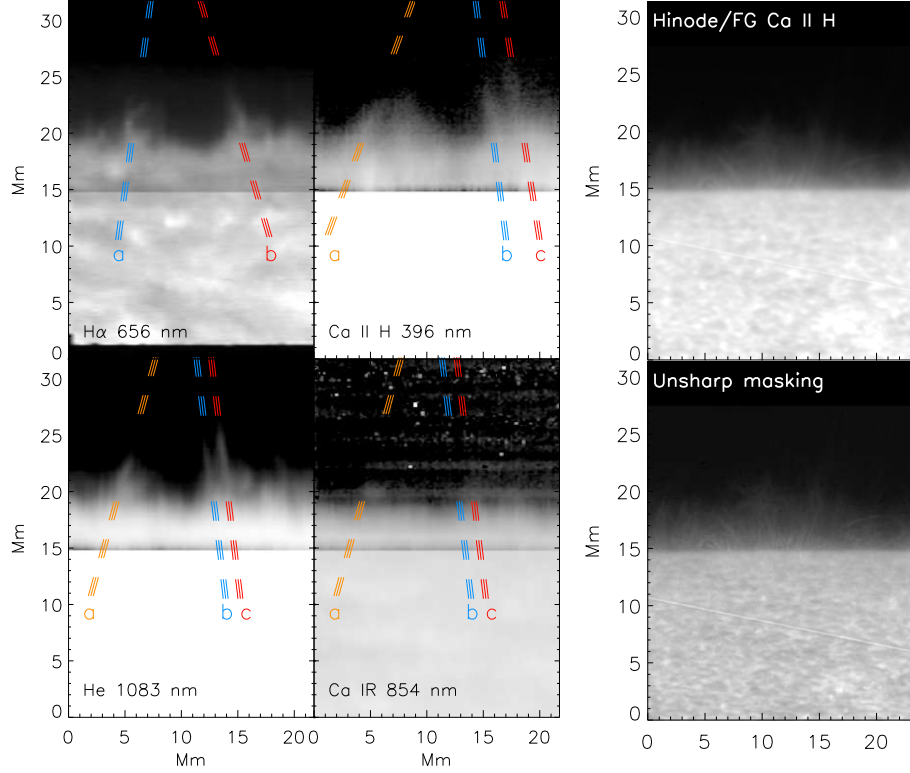


Figure 10. Left: FOV of observation No. 1 in line-core images of different spectral lines. Clockwise, starting left top: artificial $H\alpha$ scan, Ca II H , Ca II IR at 854.2 nm, and He I at 1083 nm. The inclined colored lines labeled a, b, c denote the regions over which the profiles shown in Fig. 11 were laterally averaged. The two panels at the right-hand side show an equal-sized region from a broad-band Ca II H image from Hinode without (top) and with an unsharp masking (bottom) for comparison.

$x \sim 14 \text{ Mm}$. These three lines should therefore form in a similar volume, i.e., their optical depth should be comparable and they should sample the same atmospheric volume. The line-core image of Ca II IR at 854.2 nm differs significantly from all others. The extent of emission is limited to about 5 Mm above the limb only and little to no isolated features can be identified. The two panels at the right-hand side of Fig. 10 show an equally-sized region from a broad-band Ca II H image from the Hinode filtergraph for comparison. For the bottom panel, the image was treated with an unsharp masking to enhance the contrast. The Hinode Ca image shows how the seemingly uniform emission from the limb to about 5 Mm height above it in the line-core images is composed of individual strands of spicules. The only clear examples of isolated, individual spicules in the spectra (cf. the inclined coloured lines) are found at heights where the Hinode Ca image exhibits little to no emission anymore.

To quantify the properties of the three (two in $H\alpha$) spicules in the different spectral lines, we again averaged the spectra laterally, i.e., along the x -axis, over the extent of the inclined coloured lines in Fig. 10. As before, the spicules are

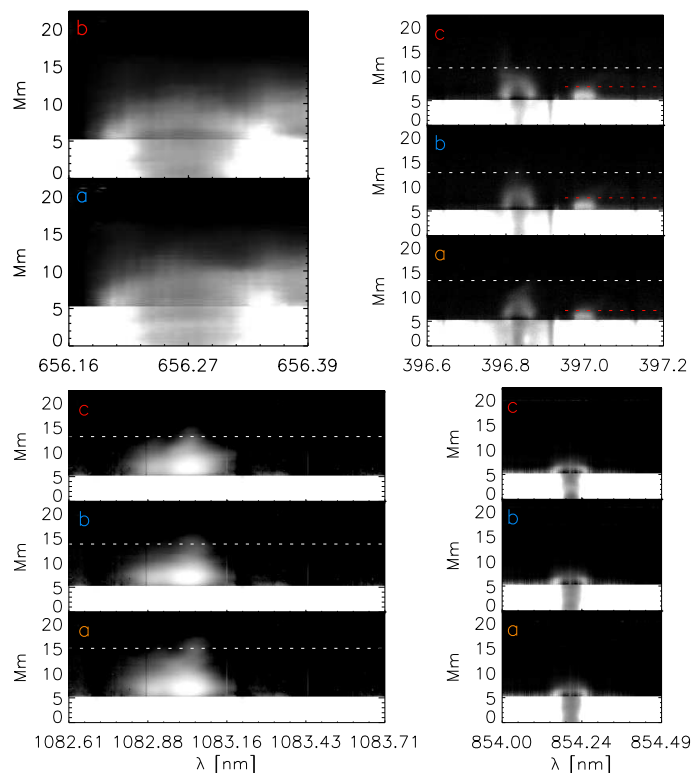


Figure 11. Laterally averaged spectra along the colored lines labeled *a, b, c* in Fig. 10. Clock-wise, starting left top: H α , Ca II H, Ca II IR at 854.2 nm, and He I at 1083 nm. The horizontal dotted lines denote the maximal height with spectra above the noise level.

nearly perpendicular to the limb, so the variation with limb distance samples the variation along the spicule length at the same time. The corresponding sets of profiles are shown in Fig. 11. All spectra are displayed on a logarithmic intensity scale to enhance the visibility of their shapes. The profile shape and its variation with height for H α and the Ca II H and IR lines is similar. The spectra show a self-absorption core close to the limb that changes a single central emission, and a decrease in line width with height (see also Pasachoff 1970; Pasachoff and Zirin 1971). For Ca II IR at 854.2 nm, the height scale of this variation is compressed by about two compared to the other lines. The He I line to the red of the Ca II H line core at 397 nm shows emission to about the same height as Ca II IR at 854.2 nm. The amplitude of emission in He I exceeds the one of Ca II H close to the limb. The shape of the He I line at 1083 nm is different from all others because of its specific formation and its being made of several components (e.g., Sánchez-Andrade Nuño *et al.* 2007), but it shows a similar trend of a reduction in line width with height.

The individual spectra of Ca II H and He I at 1083 nm for the three chosen spicules are shown in Fig. 12. For He I at 1083 nm, the line width increases up to a height of about 6 Mm, but this broadening is artificial and caused by the merging of the red and blue components of the lines. The line width decreases at

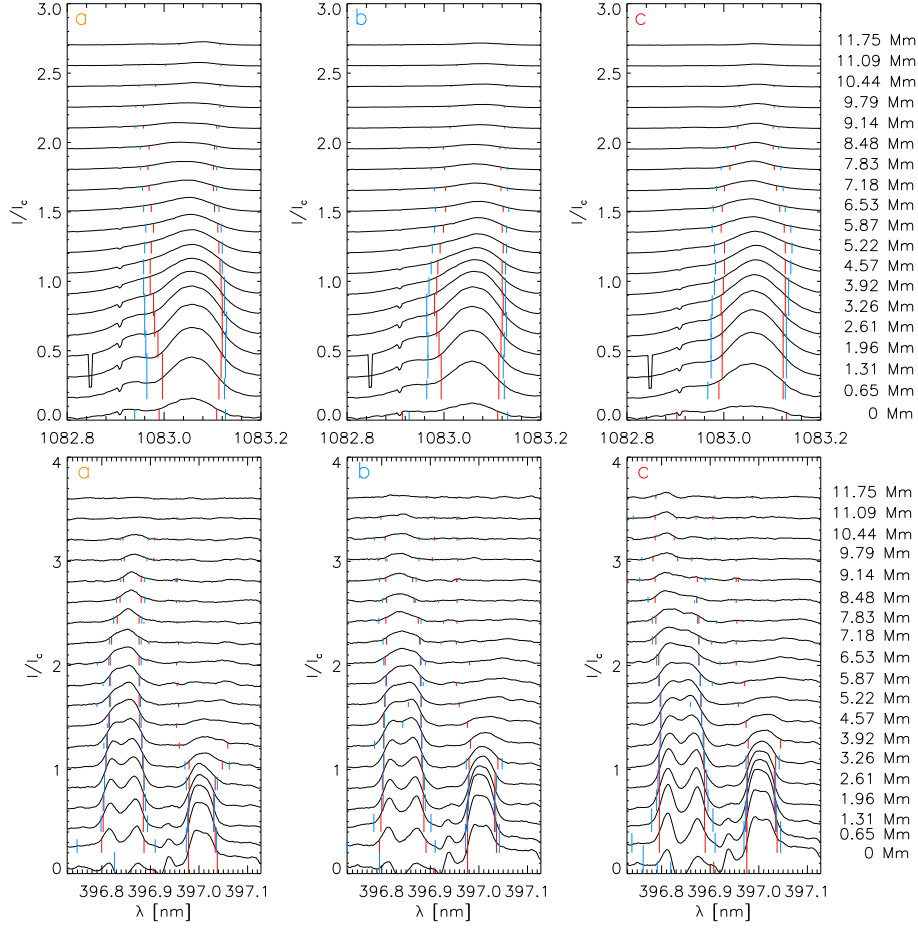


Figure 12. Laterally averaged spectra along the colored lines labeled *a, b, c* in Fig. 10. Top row: He I at 1083 nm. Bottom row: Ca II H and He I. The blue/red bars denote the FWHM from a Gaussian fit and the locations where the intensity drops to 50 % of the maximum, respectively.

larger heights. For the Ca II H spectra, the line width reduces only slightly up to about 7 to 8 Mm in all panels, but above that height the emission peak becomes significantly smaller. He I shows a different behavior, with a broadening of the line at about 3 Mm, but at the same time the intensity of the emission is already nearly zero. The spectral line seen in emission between Ca II H and He I up to a height of nearly 2 Mm should pertain to singly ionized iron (cf. Engvold and Halvorsen 1973; Lites 1974; Rutten and Stencel 1980; Watanabe and Steenbock 1986; Schmidt and Fisher 2013).

Figure 13 shows the FWHM of the laterally averaged profiles for He I at 1083 nm, Ca II H and He I. Apart from He I, the general trend is a decrease in line width with height. For He I, the line width increases on all three locations about 0.5 Mm in height before the emission has vanished completely. We note that this apparent increase in line width in He I happens at about 2–3 Mm, where all other lines indicate an usually monotonic decrease in line width.

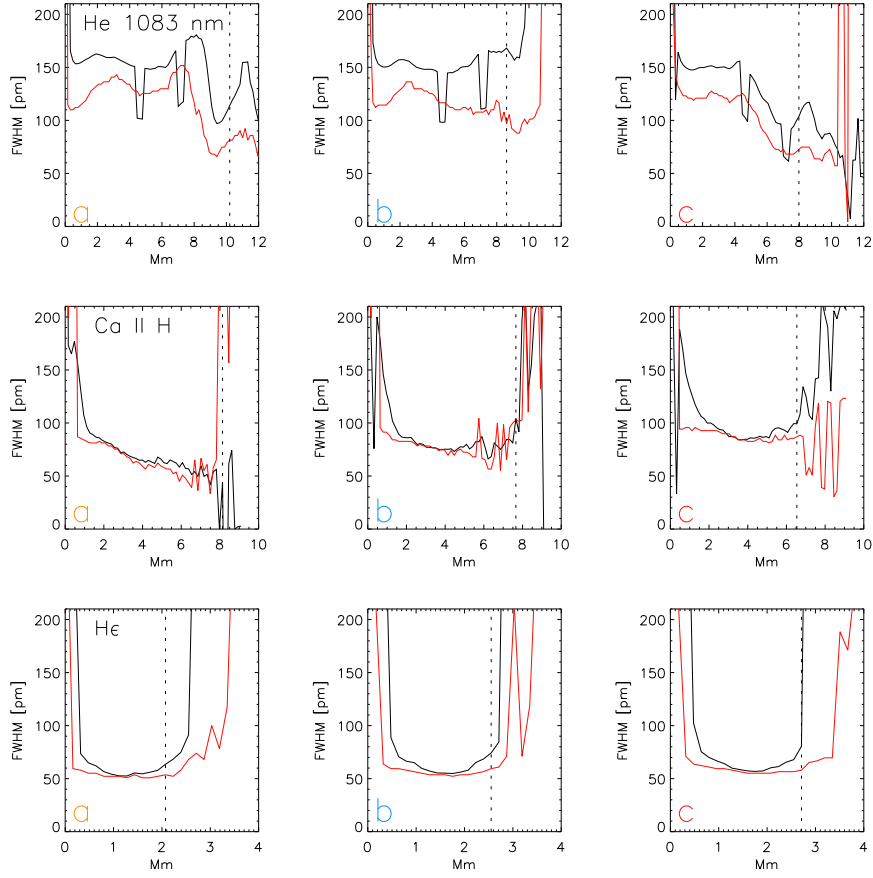


Figure 13. The FWHM of the laterally averaged spectra along the colored lines labeled *a, b, c* in Fig. 10. Black: FWHM from the Gaussian fit. Red: FWHM from the locations where the intensity drops to 50% of the maximum. The vertical dotted lines denote the maximal range with spectra above the noise level as marked in Fig. 11.

Figure 14 shows all parameters retrieved from the Gaussian fit for the He I, Ca II H and H α spectra throughout the full FOV of observation No. 1 as a cross-check of the behaviour of the line width in individual spicules. Only the off-disc area of the FOV is shown. The line width in Ca II H shows a faint lateral structuring (e.g., at $x \sim 4$ to 8 Mm), but no clear vertical variation. At best a weak trend for a reduction of the FWHM with height can be discerned. In H α , the features at $x \sim 5$ and 15 Mm show an increase of the FWHM at the upper ends, but the intensity at these places is already low. Appendix B shows in more detail that and why the values derived from these profiles are spurious, whereas the Gaussian fit works acceptably well for profiles closer to the limb. In He I, one out of the five distinct features that can be identified (two at $x \sim 5$ Mm, three at 15 Mm) shows an increase of the FWHM at the upper tip similar to those seen in H α . The FWHM increases up to the display threshold limit at the maximal

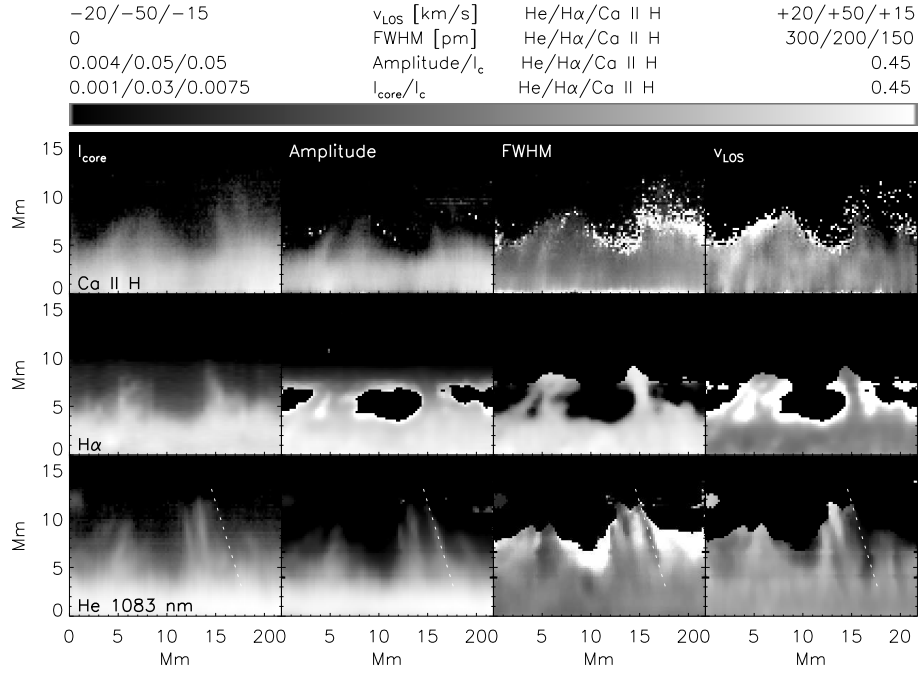


Figure 14. Results of the Gaussian fit for observation No. 1. Left to right: line-core intensity, amplitude, FWHM and LOS velocity of the fitted Gaussian. Top to bottom: Ca II H, H α , and He I at 1083 nm. The white inclined dotted line in the bottom row marks a region of reduced FWHM in He I at 1083 nm. The solar limb is at $y = 0$ Mm. The grey bar on top gives the display ranges for the respective parameters and lines.

height for which values are displayed in each column, but a comparison with the line-core intensity or the amplitude of the Gaussian reveals that these values are spurious because the intensity is nearly zero at these locations (cf. between $x \sim 7$ to 11 Mm: large FWHM (white) at $y \sim 7$ to 9 Mm coincides with nearly zero amplitude of the Gaussian). The FWHM and the LOS velocities in He I show similar patterns with more lateral fine-structure than the line-core image. The patterns of low/high FWHM or positive/negative LOS velocity are oriented similar to the spicules in the line-core images, with the same tilt relative to the limb and the same vertical extent. No clear relation between FWHM and the LOS velocities can, however, be derived instantly because all combinations of positive or negative LOS velocities with low or high FWHM can be found. The same holds for any possible relation of either FWHM or LOS velocities with high or low intensity.

Observations Nos. 2-4 are displayed in Appendix C. They yield the same result as obtained from observation No. 1: the line width decreases with increasing limb distance up to the point where the spectra show no significant emission anymore.

The spatial resolution of all of the slit-spectrograph data shown up to here was partially impeded by the limited performance of the AO system that had to operate with a facula as the main feature for the correlation. A comparison of the previous figures of the slit-spectrograph data with Fig. 15 at once shows the

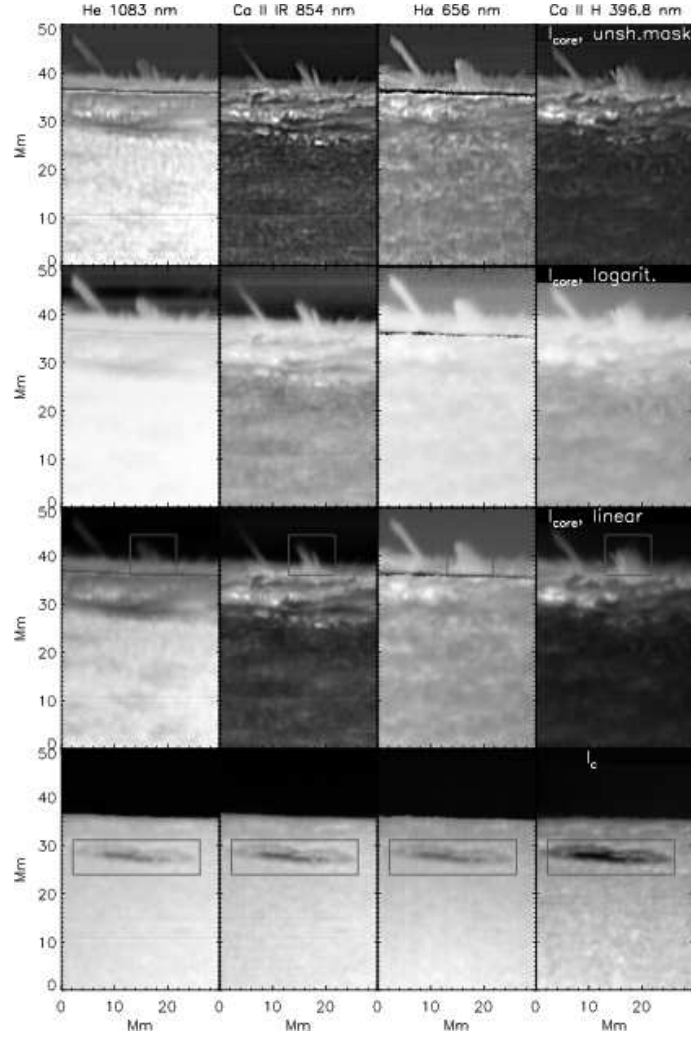


Figure 15. Overview of the FOV of observation No. 5 taken on 12/04/2011. Left to right: He I at 1083 nm, Ca II IR at 854.2 nm, H α and Ca II H. Bottom to top: continuum intensity, line-core intensity in linear display, the same in logarithmic display and the same with unsharp masking. The red rectangles outline some features in the FOV that highlight the accuracy of the spatial alignment (bottom row) and the different appearance in the line core of different spectral lines (second row from the bottom).

advantage of a better suited AO lock point such as a sunspot. Apart from the top row of Fig. 15, the images were constructed from the reduced and calibrated spectra with no additional treatment apart from the stray-light correction. These data, however, now correspond to an active region instead of the quiet Sun. The bottom row of Fig. 15 shows the continuum intensity in the full FOV in He I at 1083 nm, Ca II IR at 854.2 nm, H α and Ca II H to facilitate a control of the spatial alignment. We used the sunspot inside the red rectangle for that purpose. Because the differential refraction was again rather large early in the morning

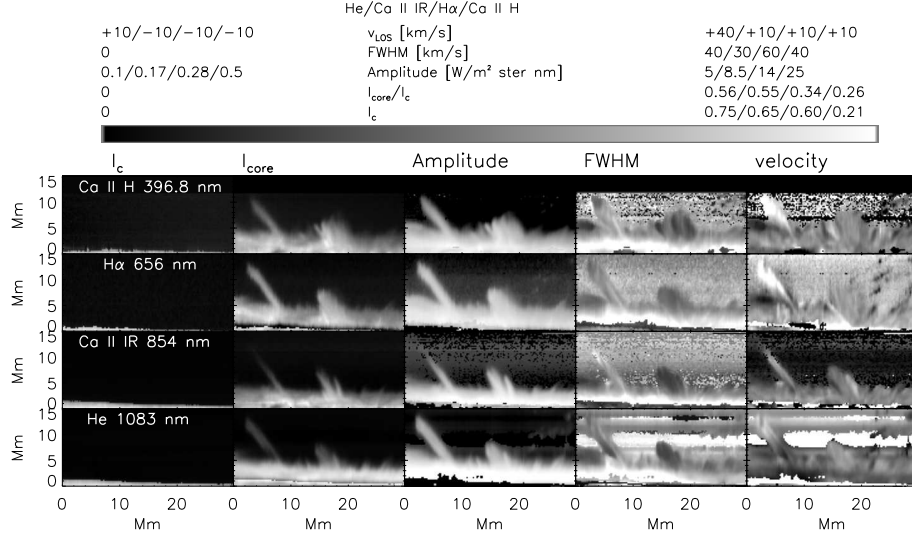


Figure 16. Results of the Gaussian fit for observation No. 5. Left to right: continuum intensity, line-core intensity, amplitude, FWHM and LOS velocity. Top to bottom: Ca II H, H α , Ca II IR at 854.2 nm and He I at 1083 nm.

when the corresponding observations were taken, the Ca II H data are less well aligned than all others, even if it is not obvious in the image. Features in the Ca II H images are at the same place after the alignment, but the corresponding Ca II H spectra were actually taken about 70 (100) s earlier than those of H α (He I).

The line-core images of Fig. 15 show several resolved spicules and macrospicules of up to 20 Mm extent at the limb. No relation of the off-limb structure to the sunspot on the disc is directly obvious, e.g., by connecting intensity brightenings or darkenings. The red rectangles in the second row from the bottom outline a cluster of spicules. Their appearance changes significantly between the different spectral lines, with both the Ca II H and the IR line showing individual strands rather than the more uniform structure seen in H α or He I at 1083 nm. The time difference between the Ca II IR and H α (He I) is zero (30 s), so the different appearance in these three lines should not be caused by the temporal evolution. The largest macrospicule at $x \sim 5$ Mm exhibits a substructure of a dark central core in the He I line-core image, whereas the corresponding bright feature in Ca II IR at 854.2 nm seems to correspond only to the central part of the macrospicule.

Figure 16 shows the results of applying the Gaussian fit to the spectra of observation No. 5. Only the off-limb region of the FOV is shown. We did not filter out the pixels without significant emission, where the results of the Gaussian fit are only spurious, as in all previous figures, because in all spectral lines the transition into noise can be clearly identified in one or all of the Gaussian parameters, best usually in the FWHM and LOS velocity. The FWHM in the cluster of spicules at $x \sim 15$ to 20 Mm is similar for H α , Ca II IR at 854.2 nm and He I at 1083 nm, but shows a much stronger lateral structuring with an iterative change from low to high FWHM in Ca II H. In all lines, the FWHM decreases or

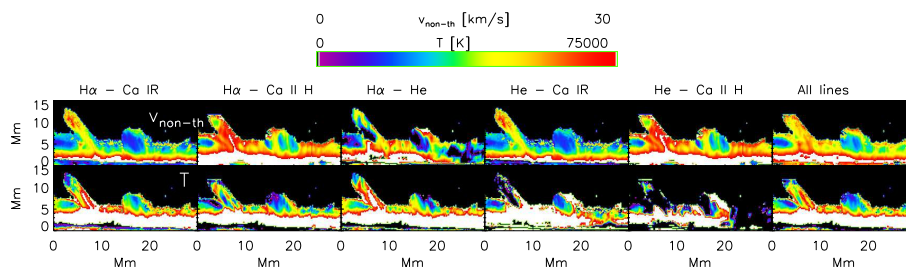


Figure 17. Kinetic temperature T_{kin} (bottom row) and non-thermal velocity $v_{\text{non-th}}$ (top row). Left to right: T_{kin} and $v_{\text{non-th}}$ from the line pairs $\text{H}\alpha - \text{Ca II IR}$, $\text{H}\alpha - \text{Ca II H}$, $\text{H}\alpha - \text{He I}$, $\text{He I} - \text{Ca II IR}$, $\text{He I} - \text{Ca II H}$ and the fit to all lines together.

remains at best constant with height above the limb for the cluster of spicules. In the largest macrospicule at $x \sim 5 \text{ Mm}$, the central axis shows an increased FWHM in all lines, and a reduction at the tip of the structure in all lines but Ca II IR at 854.2 nm .

We applied Eqs. 1 and 2 to the roughly simultaneous, co-spatial spectra of observation No. 5 to obtain an estimate of the kinetic temperature and the non-thermal line width (Fig. 17). We used all line pairs of different chemical elements and a least-square fit to all lines simultaneously (rightmost column). The different line pairs give rise to slightly different results, but some characteristics are common. The kinetic temperature in the cluster of spicules at $x \sim 18 \text{ Mm}$ ($< 30000 \text{ K}$) is lower than in the macrospicule at $x \sim 5 \text{ Mm}$ (up to above 50000 K). The temperature generally reduces towards the upper end of both structures. A similar reduction of kinetic temperature with height is to first order also seen in the rest of the FOV, especially from the layers close to the limb ($y < 5 \text{ Mm}$) towards higher layers. The non-thermal line width increases slightly at the top of the macrospicule when the Ca II IR spectra are involved, whereas for all other line pairs and combinations it reduces. The non-thermal line width is about 5 to 10 km s^{-1} in the cluster of spicules and above 15 km s^{-1} in the isolated macrospicule. Across the FOV, the non-thermal line width decreases with height similar to the kinetic temperature, with a sharp drop at a height of about 5 Mm .

4.3. Average off-limb spectra

Figures 18 and 19 show the average off-limb spectra in Ca II H , $\text{H}\alpha$, Ca II IR at 854.2 nm and He I at 1083 nm for observations No. 1 and No. 5, respectively. The $\text{H}\alpha$ spectra in Fig. 18 were taken with TESOS and therefore cover only a small wavelength range around the line core, whereas the Ca II H spectra were recorded with the PCO inside of POLIS and also include the $\text{H}\epsilon$ line. In Fig. 19, the $\text{H}\alpha$ spectra were recorded with a PCO and cover the full prefilter curve, whereas the $\text{H}\epsilon$ line was not covered in the Ca II H spectra because of using the default POLIS Ca CCD camera. The displayed wavelength range was clipped to the line-core region in all plots.

All plots from both observations show the same general trend in line width with increasing limb distance in all of the lines, i.e., the amplitude of the emission

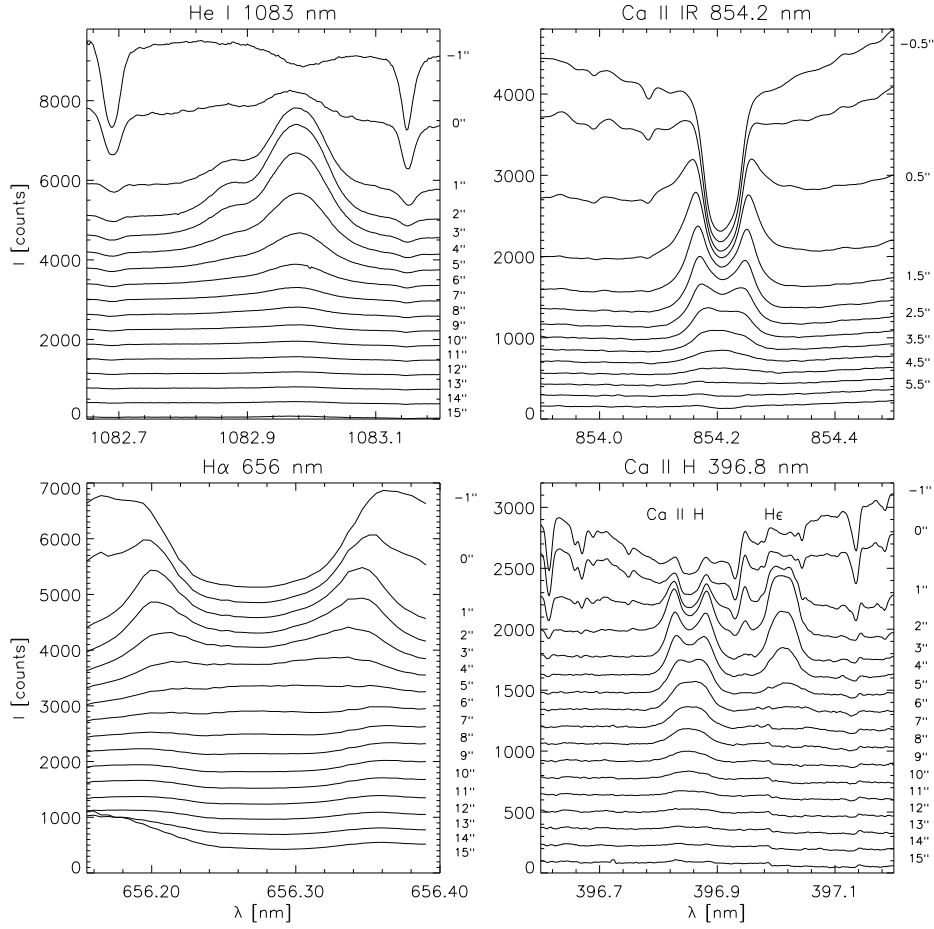


Figure 18. Average off-limb spectra of observation No.1 (cf. Fig. 10) of (clockwise, starting left top) He I 1083 nm, Ca II IR 854 nm, Ca II H and H α . The location of the profiles relative to the limb is given at the right-hand side of each panel. For Ca II IR at 854.2 nm, only profiles up to a height of 6'' are shown.

reduces strongly, making some of them virtually disappear at a height of 5 Mm, and the line width reduces up to the point where the amplitude is close to the significance limit, making the increase in line width at the uppermost heights doubtful because of the presence of some residual stray light (cf. the photospheric lines in the wings of Ca and H α). The height range where the spectra are not significant is marked by red color in the top panels and by a dotted vertical line in the bottom panels of Fig. 19, respectively. Profiles in blue show either self-absorption or are flat-topped which indicates line formation in an optically thick atmosphere (see Sect. 6.1 below).

For the data with the higher spatial resolution (observation No. 5 taken in 2011), we applied the Gaussian fit to the average profiles. The panels in the bottom row of Fig. 19 show the amplitude and the FWHM of the Gaussian for these average spectra. We extracted the line widths of the various lines from

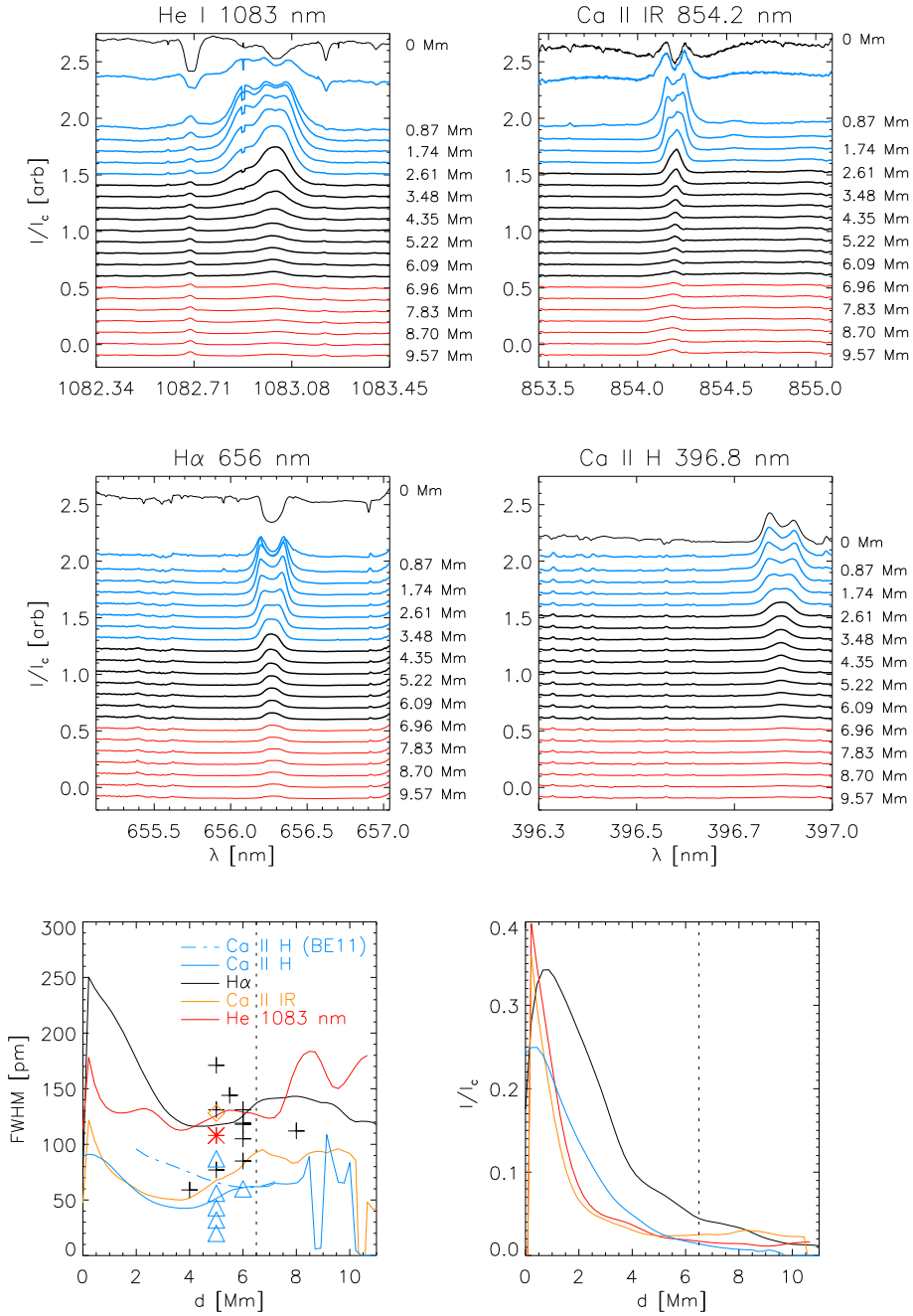


Figure 19. Top four panels: average off-limb spectra of observation No. 5 (cf. Fig. 15) of (clockwise, starting left top) He I 1083 nm, Ca II IR 854 nm, Ca II H and H α . The location of the profiles relative to the limb is given at the right-hand side of each panel. Profiles in blue show self-absorption or are flat-topped. Profiles in red are considered to represent spurious intensities. Bottom panels: FWHM (left) and amplitude (right) of the Gaussian for the average spectra. The red asterisk, orange diamond, blue triangles and black crosses denote the FWHM values of He I 1083 nm, Ca II IR 854 nm, Ca II H and H α given in Beckers (1968, 1972) and Alissandrakis (1973).

Beckers (1968, 1972) and Alissandrakis (1973) for comparison (small symbols in the lower-left panel of Fig. 19). These values show a quite significant scatter that usually covers our results for the respective lines, where our data has the advantage of having a reliable limb distance and a complete coverage of the height range up to 10 Mm above the limb. From the literature values, no clear trend in line width with height can be discerned. That the large scatter is actually a real problem caused by the use of different observations, recorded at different seeing conditions in different regions on the Sun, can be seen by comparing the line width of Ca II H with the one determined for the same line in BE11 (dash-dotted line). Using the same instrument and wavelength region, the line width retrieved in BE11 is larger than for observation No. 5 up to a height of about 6 Mm. This could be caused by either the difference between active region or quiet Sun off-limb features, or the difference in seeing with its related spatial smearing of structures at different Doppler shifts that affects the line width.

5. Summary

We have analyzed a set of multi-wavelength spectroscopic observations at the solar limb in some of the strongest chromospheric spectral lines (Ca II H at 396.85 nm, H ϵ , H α , Ca II IR at 854.2 nm and He I at 1083 nm). The setups used at the German VTT to obtain simultaneous spectra in all the lines were usually complex, making use of several instruments with additional cameras to cover more spectral lines.

We analyzed the observed spectra on two main points, i.e., the spatial structuring of the off-limb features and the line width of the spectral lines as a function of their limb distance in individual spicules, across the FOV and in average profiles. A comparison of 2D spectroscopy in H α with slit-spectrograph data in the other lines reveals that only H α and He I at 1083 nm show significant emission above a height of about 5 to 6 Mm above the solar limb. Many of the structures seen in H α above this height differ from the thin, elongated spicules seen closer to the limb, i.e., they have lateral widths of up to a few Mm and usually show complex shapes. In observations at our spatial resolution of about 1'' – apart from the GFPI data with a spatial resolution of about 0''.3 – , limb spicules merge into a dense forest without individual structure in line-core images up to a height of about 6 Mm, whereas in the Doppler velocity some spicules can still be identified at lower heights. Spicules extending above a height of 6 Mm can be seen as isolated, individual features. The lateral structuring is more pronounced than the vertical structuring, with some features maintaining their small lateral width of 1 Mm or less over a length of several Megameters. Large-scale structures in H α exhibit brightenings that propagate upwards, mostly in the form of roundish blobs. These features usually appear only in connection with large-scale, complex-shaped structures that extend beyond the typical height range of spicules.

The line width in individual spicules reduces with the height above the limb in most cases. Some lines maintain a roughly constant line width over a height range of a few Mm. We find an increase in the line width at the uppermost tips

of spicules, but its significance is doubtful because the corresponding amplitude of the emission is at the noise level of the spectra. Our results for the line width in spicules are covered by values published in previous literature, but both the literature values and our own measurements at two different times show a large scatter.

The derivation of kinetic temperatures and non-thermal velocities from the set of the best simultaneous spectra yields temperatures of about 10000 to 70000 K for spicules and macrospicules, respectively. The non-thermal velocities are between 10 and 30 km s⁻¹. These values refer, however, to off-limb structures seen near or in an active region. For our quiet Sun data, we have no equivalent set of co-spatial and simultaneous spectra because of a significant temporal shift between different wavelengths caused by the combination of differential refraction and sequential scanning. The main reason for this drawback is that the POLIS slit could not be rotated to orient it perpendicular to the horizon, while additionally the location of POLIS in the observing room of the VTT caused the largest differential refraction effects early in the morning (cf. Appendix A of Beck *et al.* 2007).

6. Discussion

For the observation of individual spicules, a high spatial resolution is required. Figures 10 and 15 demonstrate that thanks to adaptive optics, ground-based spectrograph data with an integration time of a few seconds can achieve this. The pseudo-scan map of H α in Fig. 10 additionally proves that the slit-spectrograph data correspond to a correct sampling of the temporal evolution seen in the simultaneous 2D spectroscopic data, with the limitation for their interpretation that they only cut out a single position from a temporally fast evolving 2D pattern. To preserve the spectral information, i.e., the shape of the emission and any eventual Doppler shifts, it is necessary to integrate over a few seconds because of the low light level of down to a few percent of the disc-centre intensity. Broad-band filter observations do not maintain the spectral information, but allow one to use shorter exposure or integration times. They provide the option to study the temporal evolution in detail (e.g., Pereira, De Pontieu, and Carlsson 2012) but do not allow one to extract physical properties of the solar atmosphere from the data themselves, making the review of Beckers (1968), which summarizes results of data taken before, still the reference for the physical properties of spicules.

The extraction of physical properties also depends to some extent on the availability of multiple spectral lines. The distinction between thermal and non-thermal line width, or any more detailed modeling and analysis requires more information than a single spectral lines usually provides, with the exception of the He I line at 1083 nm that in itself has several components (Sánchez-Andrade Nuño *et al.* 2007; Centeno, Trujillo Bueno, and Asensio Ramos 2010; Martínez González *et al.* 2012). Such multi-wavelength capabilities are therefore important to preserve and provide in future solar-telescope projects such as the DKIST (Rimmele *et al.* 2010) or EST (Collados *et al.* 2010). It seems that in the

last few decades similar multi-wavelength data have mainly been recorded for prominences (far) off the solar limb (e.g., Stellmacher and Wiehr 1981; Bendlin, Wiehr, and Stellmacher 1988; Stellmacher, Wiehr, and Dammasch 2003), but not for structures near and at the limb (apart from Socas-Navarro and Elmore 2005).

Stray light off the limb is an issue that needs to be dealt with in spicule observations. In the case that no direct measurements of the point-spread function are available (cf. Beck, Rezaei, and Fabbian 2011; Löfdahl and Scharmer 2012), a wavelength region in the continuum, where off the limb no solar emission is expected, can be used for the stray-light correction. For off-limb observations in chromospheric lines with 2D spectrometers such as TESOS, IBIS, CRISP or the GFPI, such a continuum wavelength point can be simply added to the spectral observation sequence to precisely determine the limb location and to correct for the off-limb stray light.

We found a limited extent of about 5 to 6 Mm above the limb for spicules, if they are defined as elongated, thin intensity streaks. Only a few isolated spicules can reach up to a height of 10 Mm. Most other features seen above 6 Mm are complex, large-scale structures with a significant lateral extent of a few Mm. There are no clear indications for any increase in line width at the tip of spicules, neither in individual spicules nor on average in the spectral lines used in our study (Ca II H, H ϵ , H α , Ca II IR at 854.2 nm, He I at 1083 nm). The same general decrease of line width in average spectra is also seen in Mg II spectra obtained with IRIS (Pereira *et al.* 2014, their Fig. 4). Structures above a height of 6 Mm do not exhibit a significantly larger line width than is seen below that height.

In our analysis of the line width, we did not try to distinguish between different types of spicular structures. This would have been possible only in the H α time-series from TESOS or the GFPI. One additional reason is that the distinction between the two types is still under debate (Zhang *et al.* 2012; Skogsrud *et al.* 2015). If the type II spicules are dominant in quiet Sun regions, they then also should have an impact on average profiles or show up prominently across the field of view (e.g., Fig. 3).

6.1. Limitations of the current analysis

Our current analysis has a few limitations for technical reasons and because of the intrinsic properties of the spectral lines observed. The low light level off the limb – actually going down to zero – introduces significant noise in the spectra. In addition, the stray light off the limb cannot be fully corrected for. The automatic analysis using a single Gaussian partly fails at emission amplitudes below 5% of I_c (Appendix B). However, the most stringent limitation is that all of the lines form in an optically thick regime in the lower part of the atmosphere. A clear indication for that is the appearance of self-absorption or flat-topped profiles (Fig. 19) because in the optically thin regime a Gaussian or Voigt profile shape should prevail. For the strong chromospheric lines (all but H ϵ), the profiles indicate an optically thick regime up to a height of about 3 Mm above the limb. Our estimates of the line width, regardless whether by the direct method or the Gaussian fit, overestimate the line width in the height range of optically

thick line formation because the true maximal emission amplitude cannot be determined. We manually fitted single Gaussians to a few profiles with clear self-absorption by forcing the amplitude of the Gaussian to be larger than the observed peak emission values and adjusting the width by hand. This yielded a line width smaller by 20 % (8 %) at a height of 2.6 Mm (3.6 Mm) above the limb than for the automated single-Gaussian fit. The general decrease in line width with height above the limb was maintained, although with a smaller slope. The best way to avoid the influence of the line formation on the derivation of line width – which is interpreted as reflecting temperature – would be a full non-local thermodynamic equilibrium modeling of spicules at different temperatures and subsequent profile synthesis as done in Judge and Carlsson (2010, e.g., their Fig. 3), but for all lines of the current observations. The interpretation of line width as temperature measure or the derivation of a kinetic temperature from the width of lines from different chemical elements come with some uncertainty (Stellmacher and Wiehr 2015).

6.2. Comparison to Rapid Blue Events

How can our finding of a decrease in line width with height above the limb be reconciled with that of Rouppe van der Voort *et al.* (2009) that rapid blue events (RBEs), the counterpart of spicules on the disc, show an increase in line width at their tips? For that, one has to take three points into account. Firstly, they found a positive correlation between blue shift and line width (e.g., their Fig. 11); secondly, one has to consider their equation to determine the line width; and finally, one has to consider the shape of the profiles they find in RBEs (e.g., their Figs. 5, 9 and 11). Their RBE profiles show clear indications of two different components: a dominating component with a small – or none at all – Doppler shift and a strongly blue-shifted satellite of lower line depth (see also Peter 2001; Tian *et al.* 2011). Their equation to determine the line width does not take the existence of the two components fully into account and corresponds more to a measure of line asymmetry than line width. Considering the line shape of the RBE profiles, the positive correlation between the velocity and the width follows directly: the larger the Doppler shift of the blue-shifted component, the larger the line asymmetry. Figure 20 shows that asymmetric RBE profiles as given in Rouppe van der Voort *et al.* (2009) can be generated without any increase in the line width in the Doppler-shifted component (compare also with the He I spectra in Figs. 12, 18 and 19 of this paper that *do* consist of two components). In the case of their RBE H α profile, one can achieve a very good reproduction of the observed profile even if the width of the Doppler-shifted component is 25 % *smaller* than that of the un-shifted component. We thus conclude that if such asymmetric profiles are typical for RBEs, they must not indicate an increased line width in the Doppler-shifted component, and hence also do not provide direct evidence for heating in RBEs.

6.3. Spicule disappearance

The rather sharp boundary in height up to which spicules reach, the change of the line shape of the spectra with height and the disappearance *in situ* can be

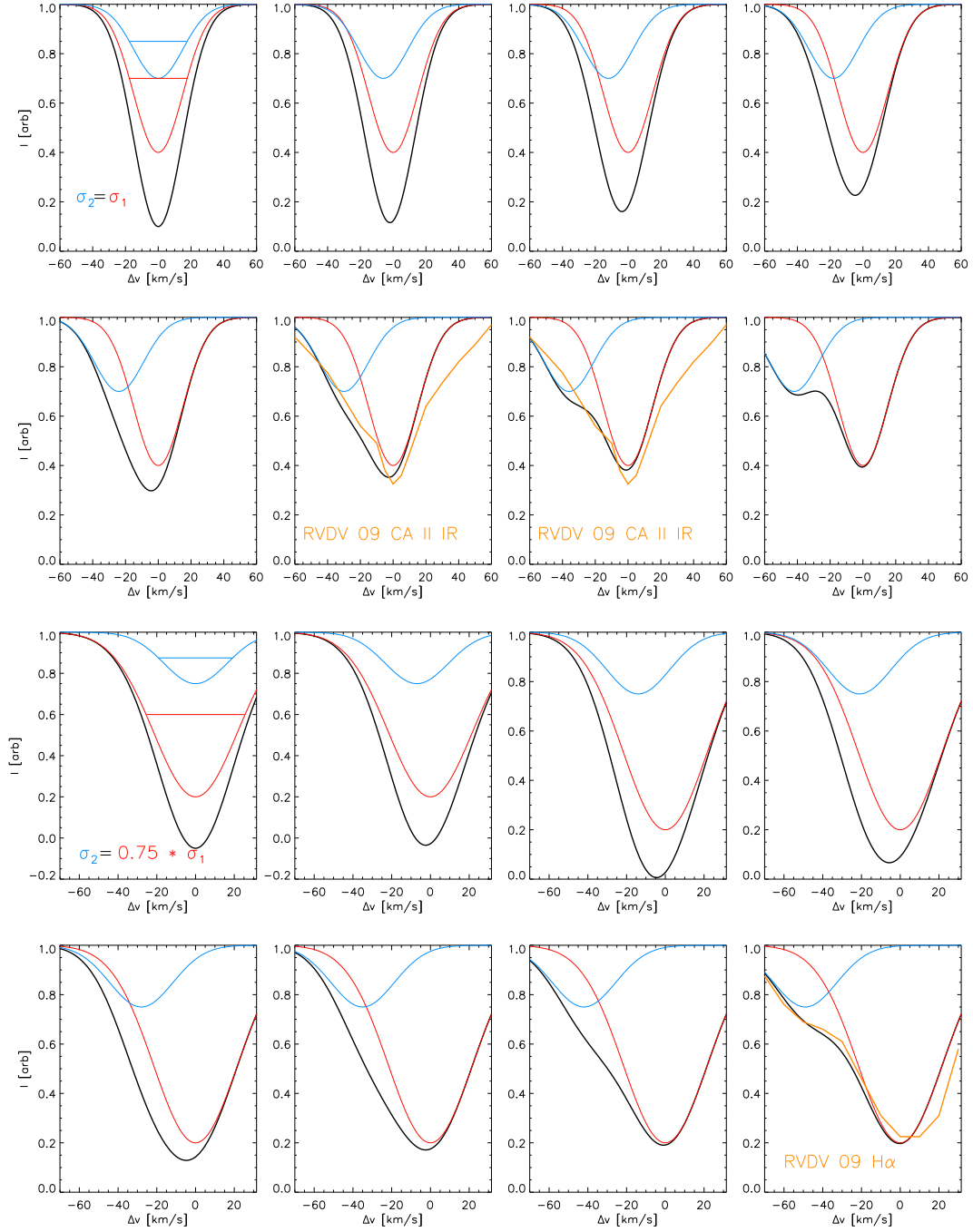


Figure 20. Reproduction of Ca II IR (top two rows) and H α (bottom two rows) profiles observed in RBEs on-disc. Two Gaussians are overlaid in each panel. The red line corresponds to an un-shifted dominant component with a width σ_1 , the blue line to a Doppler-shifted component with a width σ_2 . The Doppler shift increases from left to right in each row. The orange line corresponds to the RBE profiles of Ca II IR and H α in Fig. 11 of Rouppe van der Voort *et al.* (2009). In the case of Ca II IR, the observed profile can be reproduced to first order with Gaussians of the same width, while for H α a very good reproduction is achieved even if the width of the Doppler-shifted component is only 75% of that of the component at rest.

explained by different effects. On the one hand, the emission in the respective line cores can disappear because there is not enough material left to generate a sufficient opacity, and hence the amplitude of the emission reduces smoothly to zero (cf. Fig. 19). Because the density stratification in the quiet solar atmosphere can be assumed to be spatially rather homogeneous on large spatial or temporal scales, this would explain the sharp and well-defined upper limit in height above which almost no spicules can be seen. A second possibility is that the material would get heated strongly and rapidly such that the necessary absorbers (or emitters) are lacking because the elements that cause the spectral lines get ionized to higher ionization states. This scenario has been invoked to explain spicules that fade away *in situ* (De Pontieu *et al.* 2007a; Sterling, Moore, and DeForest 2010) and implies that spicular material could act as energy reservoir for the corona (De Pontieu *et al.* 2009, 2011). The fact that counterparts to spicules are not always found in coronal lines (e.g., Madjarska, Vanninathan, and Doyle 2011) could be by chance (but see also Klimchuk 2012). Finally, a third option would be that spicules consist of material that is shot up into the chromosphere to some height and that is hotter than the mass in the surroundings. The excess energy would then be lost by radiative cooling in the presumably optically thin environment, while the mass generally would follow a parabolic path of ascent and descent. On its path, the mass perturbation would temporally increase the density, hence the opacity and the emitted radiation would increase. That would make the travelling mass visible in the same way as prominences or coronal rain (Antolin, Vissers, and Rouppe van der Voort 2012; Oliver *et al.* 2016) show up above the solar limb. It would lead to a sequential appearance and disappearance of spicules in low-forming (Ca II) and high-forming lines (Mg II, transition region) as described in Skogsrud *et al.* (2015) in terms of a passage of the material without requiring heating.

Can our multi-line spectra be used to distinguish between these possibilities? There is one argument in favor of the reduction of density as reason for the disappearance of spicules above a height of 6 Mm, opposite to a rapid and strong heating to transition-region or coronal temperatures. The emission in both the Ca II IR line at 854.2 nm and the He I line disappears in a completely analogous way as in Ca II H, H α or He I at 1083 nm by smoothly reducing to zero with height. The former lines, however, disappear already at heights below 4 Mm (cf. Fig. 18). It is then highly unlikely that a rapid and strong heating at a height of 4 Mm would only affect these two lines without any impact on the other lines from the same chemical elements, or without changing the line width of He I at 1083 nm at this height. We thus suggest that the sharp upper boundary for the appearance of spicules, if defined as elongated, thin structures, is only the consequence of the lack of emitters caused by the reduction of density, and does not indicate a heating to transition-region temperatures.

7. Conclusions

In an analysis of multi-wavelength observations (Ca II H at 396.85 nm, He I, H α , Ca II IR at 854.2 nm and He I at 1083 nm) of solar spicules at the limb, we

find that spicules corresponding to the recently introduced type I or type II classes extend only up to a height of about 5 to 6 Mm. Structures above this height are mainly seen only in $H\alpha$, and differ by a significantly larger lateral width of up to a few Mm. All of the spectral lines show a decrease in the line width with height both in individual spicules, across the FOV and in average profiles. A slight reversal of the trend at the uppermost tips happens in spectra with very low intensities and was found to be spurious, being caused by the limitations of the data and their analysis. A derivation of the kinetic temperature and non-thermal velocities yields a decrease in both quantities with increasing limb distance. We thus find no indications that the spicules in our data are gradually or rapidly heated to transition-region or coronal temperatures or that they extend to coronal heights.

Acknowledgements The VTT is operated by the Kiepenheuer-Institut für Sonnenphysik (KIS; Freiburg, Germany) at the Spanish Observatorio del Teide of the Instituto de Astrofísica de Canarias (IAC; La Laguna, Tenerife, Spain). POLIS was a joint development of the High Altitude Observatory (HAO; Boulder, USA) and the KIS. Hinode is a Japanese mission developed and launched by ISAS/JAXA, with NAOJ as domestic partner and NASA and STFC (UK) as international partners. It is operated by these agencies in co-operation with ESA and NSC (Norway). SOHO is a project of international cooperation between ESA and NASA. HMI data are courtesy of NASA/SDO and the AIA, EVE, and HMI science teams. R.R. acknowledges financial support by the Deutsche Forschungsgemeinschaft under grant RE 3282/1-1. D. F. acknowledges financial support by the Spanish Ministries of Research and Innovation and of Economy through projects AYA2011-24808 and CSD2007-00050.

References

- Alissandrakis, C.E.: 1973, A Spectroscopic Study of Solar Spicules in $H\alpha$, $H\beta$ and K. *Solar Phys.* **32**, 345. DOI. ADS.
- Anan, T., Kitai, R., Kawate, T., Matsumoto, T., Ichimoto, K., Shibata, K., Hillier, A., Otsuji, K., Watanabe, H., Ueno, S., Nagata, S., Ishii, T.T., Komori, H., Nishida, K., Nakamura, T., Isobe, H., Hagino, M.: 2010, Spicule Dynamics over a Plage Region. *Pub. Astron. Soc. Japan* **62**. ADS.
- Antolin, P., Vissers, G., Rouppe van der Voort, L.: 2012, On-Disk Coronal Rain. *Solar Phys.* **280**, 457. DOI. ADS.
- Athay, R.G.: 2000, Are Spicules Related to Coronal Heating? *Solar Phys.* **197**, 31. ADS.
- Athay, R.G., Holzer, T.E.: 1982, The role of spicules in heating the solar atmosphere. *Astrophys. J.* **255**, 743. DOI. ADS.
- Avery, L.W.: 1970, The formation of the Ca ii K line in a spinning spicule. *Solar Phys.* **13**, 301. DOI. ADS.
- Beck, C., Rezaei, R.: 2012, Chromospheric Multi-Wavelength Observations near the Solar Limb: Techniques and Prospects. In: Rimmele, T.R., Tritschler, A., Wöger, F., Collados Vera, M., Socas-Navarro, H., Schlichenmaier, R., Carlsson, M., Berger, T., Cadavid, A., Gilbert, P.R., Goode, P.R., Knölker, M. (eds.) *Magnetic Fields from the Photosphere to the Corona*, *ASP Conference Series* **463**, 257. ADS.
- Beck, C., Rezaei, R., Fabbian, D.: 2011, Stray-light contamination and spatial deconvolution of slit-spectrograph observations. *Astron. Astrophys.* **535**, A129. DOI. ADS.

- Beck, C., Rezaei, R., Puschmann, K.G.: 2013, Can spicules be detected at disc centre in broad-band Ca ii H filter imaging data? *Astron. Astrophys.* **556**, A127. DOI. ADS.
- Beck, C.A.R., Rezaei, R.: 2011, Spectroscopy at the solar limb. I. Average off-limb profiles and Doppler shifts of Ca II H. *Astron. Astrophys.* **531**, A173. DOI. ADS.
- Beck, C., Schmidt, W., Kentischer, T., Elmore, D.: 2005, Polarimetric Littrow Spectrograph - instrument calibration and first measurements. *Astron. Astrophys.* **437**, 1159. DOI. ADS.
- Beck, C., Bellot Rubio, L.R., Schlichenmaier, R., Sütterlin, P.: 2007, Magnetic properties of G-band bright points in a sunspot moat. *Astron. Astrophys.* **472**, 607. DOI. ADS.
- Beck, C., Schmidt, W., Rezaei, R., Rammacher, W.: 2008, The signature of chromospheric heating in Ca II H spectra. *Astron. Astrophys.* **479**, 213. DOI.
- Beck, C., Fabbian, D., Moreno-Insertis, F., Puschmann, K.G., Rezaei, R.: 2013, Thermodynamic fluctuations in solar photospheric three-dimensional convection simulations and observations. *Astron. Astrophys.* **557**, A109. DOI. ADS.
- Beckers, J.M.: 1968, Solar Spicules (Invited Review Paper). *Solar Phys.* **3**, 367.
- Beckers, J.M.: 1972, Solar Spicules. *ARA&A* **10**, 73.
- Bendlin, C., Wiehr, E., Stellmacher, G.: 1988, Spectroscopic analysis of prominence emissions. *Astron. Astrophys.* **197**, 274. ADS.
- Berger, T.E., Shine, R.A., Slater, G.L., Tarbell, T.D., Title, A.M., Okamoto, T.J., Ichimoto, K., Katsukawa, Y., Suematsu, Y., Tsuneta, S., Lites, B.W., Shimizu, T.: 2008, Hinode SOT Observations of Solar Quiescent Prominence Dynamics. *Astrophys. J. Lett.* **676**, L89. DOI. ADS.
- Bohlin, J.D., Vogel, S.N., Purcell, J.D., Sheeley, N.R. Jr., Tousey, R., Vanhoosier, M.E.: 1975, A newly observed solar feature - Macrospicules in He II 304 Å. *Astrophys. J. Lett.* **197**, L133. DOI. ADS.
- Cabrera Solana, D., Bellot Rubio, L.R., Beck, C., Del Toro Iniesta, J.C.: 2007, Temporal evolution of the Evershed flow in sunspots. I. Observational characterization of Evershed clouds. *Astron. Astrophys.* **475**, 1067. DOI.
- Casini, R., López Ariste, A., Tomczyk, S., Lites, B.W.: 2003, Magnetic Maps of Prominences from Full Stokes Analysis of the He I D3 Line. *Astrophys. J. Lett.* **598**, L67. DOI. ADS.
- Cavallini, F.: 2006, IBIS: A New Post-Focus Instrument for Solar Imaging Spectroscopy. *Solar Phys.* **236**, 415. DOI. ADS.
- Centeno, R., Trujillo Bueno, J., Asensio Ramos, A.: 2010, On the Magnetic Field of Off-limb Spicules. *Astrophys. J.* **708**, 1579. DOI. ADS.
- Collados, M., Lagg, A., Díaz García, J.J., Hernández Suárez, E., López López, R., Páez Mañá, E., Solanki, S.K.: 2007, Tenerife Infrared Polarimeter II. In: Heinzel, P., Dorotović, I., Rutten, R.J. (eds.) *The Physics of Chromospheric Plasmas*, *ASP Conference Series* **368**, 611. ADS.
- Collados, M., Bettonvil, F., Cavaller, L., Ermolli, I., Gelly, B., Grivel-Gelly, C., Pérez, A., Socas-Navarro, H., Soltau, D., Volkmer, R.: 2010, European Solar Telescope: project status. In: Stepp, L.M., R., G., Hall, H.J. (eds.) *Ground-based and Airborne Telescopes III, Society of Photo-Optical Instrumentation Engineers (SPIE) Conference Series* **7733**, 77330H. DOI. ADS.
- De Pontieu, B., Haerendel, G.: 1998, Weakly damped Alfvén waves as drivers for spicules. *Astron. Astrophys.* **338**, 729.
- De Pontieu, B., Erdélyi, R., James, S.P.: 2004, Solar chromospheric spicules from the leakage of photospheric oscillations and flows. *Nature* **430**, 536. DOI.
- De Pontieu, B., McIntosh, S., Hansteen, V.H., Carlsson, M., Schrijver, C.J., Tarbell, T.D., Title, A.M., Shine, R.A., Suematsu, Y., Tsuneta, S., Katsukawa, Y., Ichimoto, K., Shimizu, T., Nagata, S.: 2007a, A Tale of Two Spicules: The Impact of Spicules on the Magnetic Chromosphere. *Pub. Astron. Soc. Japan* **59**, 655.
- De Pontieu, B., Hansteen, V.H., Rouppe van der Voort, L., van Noort, M., Carlsson, M.: 2007b, High-Resolution Observations and Modeling of Dynamic Fibrils. *Astrophys. J.* **655**, 624. DOI.
- De Pontieu, B., McIntosh, S.W., Hansteen, V.H., Schrijver, C.J.: 2009, Observing the Roots of Solar Coronal Heating in the Chromosphere. *Astrophys. J. Lett.* **701**, L1. DOI. ADS.
- De Pontieu, B., McIntosh, S.W., Carlsson, M., Hansteen, V.H., Tarbell, T.D., Boerner, P., Martinez-Sykora, J., Schrijver, C.J., Title, A.M.: 2011, The Origins of Hot Plasma in the Solar Corona. *Science* **331**. DOI. ADS.
- De Pontieu, B., Carlsson, M., Rouppe van der Voort, L.H.M., Rutten, R.J., Hansteen, V.H., Watanabe, H.: 2012, Ubiquitous Torsional Motions in Type II Spicules. *Astrophys. J. Lett.* **752**, L12. DOI. ADS.

- Engvold, O., Halvorsen, H.D.: 1973, New identifications of disk emission lines in the Ca ii H and K line wings. *Solar Phys.* **28**, 23. DOI. ADS.
- Felipe, T., Khomenko, E., Collados, M., Beck, C.: 2010, Multi-layer Study of Wave Propagation in Sunspots. *Astrophys. J.* **722**, 131. DOI. ADS.
- Gandorfer, A.M., Steiner, H.P.P.P., Aebbersold, F., Egger, U., Feller, A., Gisler, D., Hagenbuch, S., Stenflo, J.O.: 2004, Solar polarimetry in the near UV with the Zurich Imaging Polarimeter ZIMPOL II. *Astron. Astrophys.* **422**, 703. DOI. ADS.
- Goodman, M.L.: 2012, Acceleration of Type II Spicules in the Solar Chromosphere. *Astrophys. J.* **757**, 188. DOI. ADS.
- Grossmann-Doerth, U., Schmidt, W.: 1992, Chromospheric fine structure revisited. *Astron. Astrophys.* **264**, 236.
- Guerreiro, N., Carlsson, M., Hansteen, V.: 2013, Numerical Simulations of Spicule Acceleration. *Astrophys. J.* **766**, 128. DOI. ADS.
- Hammer, R., Musielak, Z.E., Routh, S., Nesis, A.: 2008, Spicules: Energetics and the Role of Magnetic Waves. *12th European Solar Physics Meeting, Freiburg, Germany, held September, 8-12, 2008* **12**, 3.
- Hansteen, V.H., De Pontieu, B., Rouppe van der Voort, L., van Noort, M., Carlsson, M.: 2006, Dynamic Fibrils Are Driven by Magnetoacoustic Shocks. *Astrophys. J. Lett.* **647**, L73. DOI.
- He, J., Tu, C., Marsch, E., Guo, L., Yao, S., Tian, H.: 2009, Upward propagating high-frequency Alfvén waves as identified from dynamic wave-like spicules observed by SOT on Hinode. *Astron. Astrophys.* **497**, 525.
- Heggland, L., De Pontieu, B., Hansteen, V.H.: 2009, Observational Signatures of Simulated Reconnection Events in the Solar Chromosphere and Transition Region. *Astrophys. J.* **702**, 1. DOI. ADS.
- Hollweg, J.V.: 1982, On the origin of solar spicules. *Astrophys. J.* **257**, 345. DOI. ADS.
- Jess, D.B., Mathioudakis, M., Christian, D.J., Keenan, F.P., Ryans, R.S.I., Crockett, P.J.: 2010, ROSA: A High-Cadence, Synchronized Multi-camera Solar Imaging System. *Solar Phys.* **261**, 363.
- Jess, D.B., Pascoe, D.J., Christian, D.J., Mathioudakis, M., Keys, P.H., Keenan, F.P.: 2012, The origin of type I spicule oscillations. *Astrophys. J. Lett.* **744**, L5.
- Judge, P.G., Carlsson, M.: 2010, On the Solar Chromosphere Observed at the LIMB with Hinode. *Astrophys. J.* **719**, 469. DOI. ADS.
- Judge, P.G., de Pontieu, B., McIntosh, S.W., Olluri, K.: 2012, The Connection of Type II Spicules to the Corona. *Astrophys. J.* **746**, 158. DOI. ADS.
- Kamio, S., Curdt, W., Teriaca, L., Inhester, B., Solanki, S.K.: 2010, Observations of a rotating macrospicule associated with an X-ray jet. *Astron. Astrophys.* **510**, L1. DOI.
- Kentischer, T.J., Schmidt, W., Sigwarth, M., von Uexküll, M.: 1998, TESOS, a double Fabry-Perot instrument for solar spectroscopy. *Astron. Astrophys.* **340**, 569.
- Klimchuk, J.A.: 2012, The role of type II spicules in the upper solar atmosphere. *Journal of Geophysical Research (Space Physics)* **117**(A16), 12102. DOI. ADS.
- Kosugi, T., Matsuzaki, K., Sakao, T., Shimizu, T., Sone, Y., Tachikawa, S., Hashimoto, T., Minesugi, K., Ohnishi, A., Yamada, T., Tsuneta, S., Hara, H., Ichimoto, K., Suematsu, Y., Shimojo, M., Watanabe, T., Shimada, S., Davis, J.M., Hill, L.D., Owens, J.K., Title, A.M., Culhane, J.L., Harra, L.K., Doschek, G.A., Golub, L.: 2007, The Hinode (Solar-B) Mission: An Overview. *Solar Phys.* **243**, 3. DOI. ADS.
- Kudoh, T., Shibata, K.: 1999, Alfvén Wave Model of Spicules and Coronal Heating. *Astrophys. J.* **514**, 493. DOI. ADS.
- Kukhianidze, V., Zaqarashvili, T.V., Khutsishvili, E.: 2006, Observation of kink waves in solar spicules. *Astron. Astrophys.* **449**, L35. DOI.
- Kulidzanishvili, V.I., Zhugzhda, I.D.: 1983, On the problem of spicular oscillations. *Solar Phys.* **88**, 35. DOI. ADS.
- Kurucz, R.L., Furenlid, I., Brault, J., Testerman, L.: 1984, *Solar flux atlas from 296 to 1300 nm*. ADS.
- Langangen, Ø., De Pontieu, B., Carlsson, M., Hansteen, V.H., Cauzzi, G., Reardon, K.: 2008, Search for High Velocities in the Disk Counterpart of Type II Spicules. *Astrophys. J. Lett.* **679**, L167. DOI. ADS.
- Lites, B.W.: 1974, The Solar Fen 2L 3969. 4 Disk Emission Line. *Astron. Astrophys.* **33**, 363. ADS.

- Löfdahl, M.G.: 2002, Multi-frame blind deconvolution with linear equality constraints. In: P.J. Bones et al. (ed.) *Image Reconstruction from Incomplete Data II, SPIE Conference Series*, 4792.
- Löfdahl, M.G., Scharmer, G.B.: 2012, Sources of straylight in the post-focus imaging instrumentation of the Swedish 1-m Solar Telescope. *Astron. Astrophys.* **537**, A80. DOI. ADS.
- López Ariste, A., Casini, R.: 2005, Inference of the magnetic field in spicules from spectropolarimetry of He I D3. *Astron. Astrophys.* **436**, 325. DOI.
- López Ariste, A., Rayrole, J., Semel, M.: 2000, First results from THEMIS spectropolarimetric mode. *A&AS* **142**, 137. DOI.
- Madjarska, M.S., Vanninathan, K., Doyle, J.G.: 2011, Can coronal hole spicules reach coronal temperatures? *Astron. Astrophys.* **532**, L1. DOI. ADS.
- Makita, M.: 2003, Chromospheric structure derived from flash spectra of the total solar eclipse. *Publications of the National Astronomical Observatory of Japan* **7**, 1. ADS.
- Martínez González, M.J., Asensio Ramos, A., Manso Sainz, R., Beck, C., Belluzzi, L.: 2012, Anomalous Circular Polarization Profiles in the He I 1083.0 nm Multiplet from Solar Spicules. *Astrophys. J.* **759**, 16. DOI. ADS.
- Martinez Pillet, V.: 1992, Stray-light effects on the solar intensity distribution. *Solar Phys.* **140**, 207. DOI. ADS.
- Martínez Pillet, V., Collados, M., Sánchez Almeida, J., González, V., Cruz-Lopez, A., Manescau, A., Joven, E., Paez, E., Diaz, J., Feeney, O., Sánchez, V., Scharmer, G., Soltau, D.: 1999, LPSP & TIP: Full Stokes Polarimeters for the Canary Islands Observatories. In: T. R. Rimmele, K. S. Balasubramaniam, & R. R. Radick (ed.) *High Resolution Solar Physics: Theory, Observations, and Techniques, ASP Conference Series* **183**, 264. ADS.
- Martínez-Sykora, J., Hansteen, V., Moreno-Inertis, F.: 2011, On the Origin of the Type II Spicules: Dynamic Three-dimensional MHD Simulations. *Astrophys. J.* **736**, 9. DOI. ADS.
- Martínez-Sykora, J., Hansteen, V., DePontieu, B., Carlsson, M.: 2009, Spicule-Like Structures Observed in Three-Dimensional Realistic Magnetohydrodynamic Simulations. *Astrophys. J.* **701**, 1569. DOI. ADS.
- Matsuno, K., Hirayama, T.: 1988, The height distribution of the kinetic temperature and turbulent velocity of solar H α spicules. *Solar Phys.* **117**, 21.
- Mattig, W.: 1983, On the instrumental and atmospheric stray-light for solar observations. *Solar Phys.* **87**, 187. DOI. ADS.
- McIntosh, S.W., De Pontieu, B.: 2009, Observing Episodic Coronal Heating Events Rooted in Chromospheric Activity. *Astrophys. J. Lett.* **706**, L80. DOI. ADS.
- Murawski, K., Srivastava, A.K., Zaqarashvili, T.V.: 2011, Numerical simulations of solar macropicules. *Astron. Astrophys.* **535**, A58. DOI. ADS.
- Neckel, H.: 1999, Announcement. *Solar Phys.* **184**, 421. ADS.
- Nishikawa, T.: 1988, Spicule observations with high spatial resolution. *Pub. Astron. Soc. Japan* **40**, 613.
- Oliver, R., Soler, R., Terradas, J., Zaqarashvili, T.V.: 2016, Dynamics of Coronal Rain and Descending Plasma Blobs in Solar Prominences. II. Partially Ionized Case. *Astrophys. J.* **818**, 128. DOI. ADS.
- Orozco Suárez, D., Asensio Ramos, A., Trujillo Bueno, J.: 2015, Height Variation of the Vector Magnetic Field in Solar Spicules. *Astrophys. J. Lett.* **803**, L18. DOI. ADS.
- Paletou, F., López Ariste, A., Bommier, V., Semel, M.: 2001, Full-Stokes spectropolarimetry of solar prominences. *Astron. Astrophys.* **375**, L39. DOI.
- Pasachoff, J.M.: 1970, Fine structure in Ca II on the solar disc. *Solar Phys.* **12**, 202.
- Pasachoff, J.M., Zirin, H.: 1971, On K-line central reversals. *Solar Phys.* **18**, 27.
- Pasachoff, J.M., Jacobson, W.A., Sterling, A.C.: 2009, Limb Spicules from the Ground and from Space. *Solar Phys.* **260**, 59.
- Pasachoff, J.M., Noyes, R.W., Beckers, J.M.: 1968, Spectral Observations of Spicules at Two Heights in the Solar Chromosphere. *Solar Phys.* **5**, 131. DOI. ADS.
- Pereira, T.M.D., De Pontieu, B., Carlsson, M.: 2012, Quantifying Spicules. *Astrophys. J.* **759**, 18. DOI. ADS.
- Pereira, T.M.D., De Pontieu, B., Carlsson, M.: 2013, The Effects of Spatio-temporal Resolution on Deduced Spicule Properties. *Astrophys. J.* **764**, 69. DOI. ADS.
- Pereira, T.M.D., De Pontieu, B., Carlsson, M., Hansteen, V., Tarbell, T.D., Lemen, J., Title, A., Boerner, P., Hurlburt, N., Wülser, J.P., Martínez-Sykora, J., Kleint, L., Golub, L., McKillop, S., Reeves, K.K., Saar, S., Testa, P., Tian, H., Jaeggli, S., Kankelborg, C.: 2014,

- An Interface Region Imaging Spectrograph First View on Solar Spicules. *Astrophys. J. Lett.* **792**, L15. DOI. ADS.
- Peter, H.: 2001, On the nature of the transition region from the chromosphere to the corona of the Sun. *Astron. Astrophys.* **374**, 1108. DOI. ADS.
- Pike, C.D., Harrison, R.A.: 1997, EUV Observations of a Macrospicule: Evidence for Solar Wind Acceleration? *Solar Phys.* **175**, 457. DOI. ADS.
- Pneuman, G.W., Kopp, R.A.: 1978, Downflow in the supergranulation network and its implications for transition region models. *Solar Phys.* **57**, 49. DOI. ADS.
- Puschmann, K.G.: 2016, Spicules and their on-disk counterparts, the main driver for solar chromospheric heating? *ArXiv e-prints*. ADS.
- Puschmann, K.G., Beck, C.: 2011, Application of speckle and (multi-object) multi-frame blind deconvolution techniques on imaging and imaging spectropolarimetric data. *Astron. Astrophys.* **533**, A21. DOI. ADS.
- Puschmann, K.G., Kneer, F., Seelemann, T., Wittmann, A.D.: 2006, The new Göttingen Fabry-Pérot spectrometer for two-dimensional observations of the Sun. *Astron. Astrophys.* **451**, 1151. DOI.
- Puschmann, K.G., Kneer, F., Nicklas, H., Wittmann, A.D.: 2007, From the "Göttingen" Fabry-Pérot Interferometer to the GREGOR FPI. In: Kneer, F., Puschmann, K.G., Wittmann, A.D. (eds.) *Modern solar facilities - advanced solar science*, 45. ADS.
- Puschmann, K.G., Denker, C., Kneer, F., Al Erdogan, N., Balthasar, H., Bauer, S.M., Beck, C., Bello González, N., Collados, M., Hahn, T., Hirzberger, J., Hofmann, A., Louis, R.E., Nicklas, H., Okunev, O., Martínez Pillet, V., Popow, E., Seelemann, T., Volkmer, R., Wittmann, A.D., Woche, M.: 2012a, The GREGOR Fabry-Pérot Interferometer. *Astronomische Nachrichten* **333**, 880. DOI. ADS.
- Puschmann, K.G., Balthasar, H., Bauer, S.-M., Hahn, T., Popow, E., Seelemann, T., Volkmer, R., Woche, M., Denker, C.: 2012b, The GREGOR Fabry-Pérot Interferometer: A New Instrument for High-Resolution Spectropolarimetric Solar Observations. In: Rimmele, T.R., Tritschler, A., Wöger, F., Collados Vera, M., Socas-Navarro, H., Schlichenmaier, R., Carlsson, M., Berger, T., Cadavid, A., Gilbert, P.R., Goode, P.R., Knölker, M. (eds.) *The Second ATST-EAST Meeting: Magnetic Fields from the Photosphere to the Corona, ASP Conference Series* **463**, 423. ADS.
- Puschmann, K.G., Balthasar, H., Beck, C., Louis, R.E., Popow, E., Seelemann, T., Volkmer, R., Woche, M., Denker, C.: 2012c, The GREGOR Fabry-Pérot interferometer: status report and prospects. In: *Ground-based and Airborne Instrumentation for Astronomy IV, Society of Photo-Optical Instrumentation Engineers (SPIE) Conference Series* **8446**, 79. DOI. ADS.
- Puschmann, K.G., Denker, C., Balthasar, H., Louis, R.E., Popow, E., Woche, M., Beck, C., Seelemann, T., Volkmer, R.: 2013, GREGOR Fabry-Pérot interferometer and its companion the blue imaging solar spectrometer. *Optical Engineering* **52**(8), 081606. DOI. ADS.
- Ramelli, R., Bianda, M., Merenda, L., Trujillo Bueno, T.: 2006, The Hanle and Zeeman Effects in Solar Spicules. In: R. Casini & B. W. Lites (ed.) *Proceedings of SPW4, ASP Conference Series* **358**, 448. ADS.
- Reardon, K.P., Cavallini, F.: 2008, Characterization of Fabry-Pérot interferometers and multi-etalon transmission profiles. The IBIS instrumental profile. *Astron. Astrophys.* **481**, 897. DOI.
- Rimmele, T.R., Wagner, J., Keil, S., Elmore, D., Hubbard, R., Hansen, E., Warner, M., Jeffers, P., Phelps, L., Marshall, H., Goodrich, B., Richards, K., Hegwer, S., Kneale, R., Ditsler, J.: 2010, The Advanced Technology Solar Telescope: beginning construction of the world's largest solar telescope. In: Stepp, L.M., R., G., Hall, H.J. (eds.) *Ground-based and Airborne Telescopes III., Society of Photo-Optical Instrumentation Engineers (SPIE) Conference Series* **7733**. DOI. ADS.
- Roberts, W.O.: 1945, A Preliminary Report on Chromospheric Spicules of Extremely Short Lifetime. *Astrophys. J.* **101**, 136. DOI. ADS.
- Roupe van der Voort, L.H.M., De Pontieu, B., Hansteen, V.H., Carlsson, M., van Noort, M.: 2007, Magnetoacoustic Shocks as a Driver of Quiet-Sun Mottles. *Astrophys. J. Lett.* **660**, L169. DOI.
- Roupe van der Voort, L., Leenaarts, J., de Pontieu, B., Carlsson, M., Vissers, G.: 2009, On-disk Counterparts of Type II Spicules in the Ca II 854.2 nm and H α Lines. *Astrophys. J.* **705**, 272.
- Roupe van der Voort, L., De Pontieu, B., Pereira, T.M.D., Carlsson, M., Hansteen, V.: 2015, Heating Signatures in the Disk Counterparts of Solar Spicules in Interface Region Imaging Spectrograph Observations. *Astrophys. J. Lett.* **799**, L3. DOI. ADS.

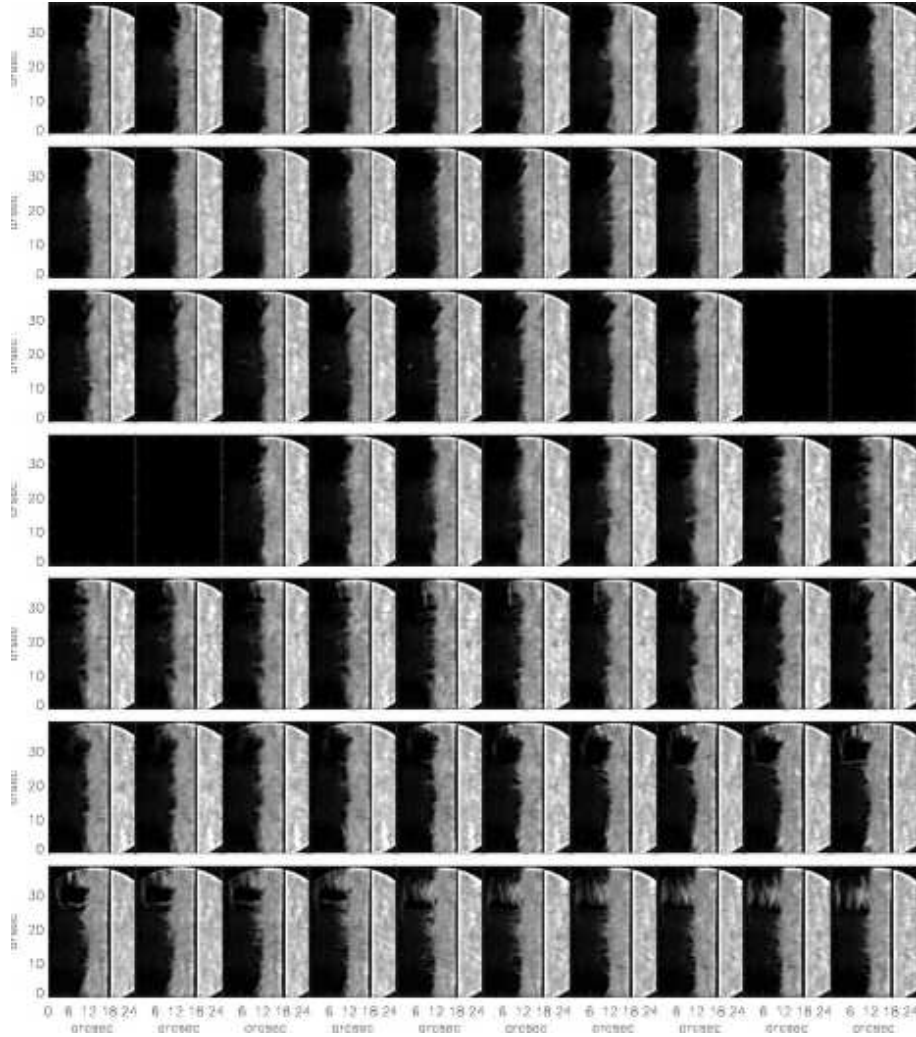
- Rutten, R.J., Stencel, R.E.: 1980, Solar limb emission lines near CA II H & K and their spatial intensity variations. *Astron. Astrophys. Suppl.* **39**, 415. ADS.
- Sánchez-Andrade Nuño, B., Centeno, R., Puschmann, K.G., Trujillo Bueno, J., Blanco Rodríguez, J., Kneer, F.: 2007, Spicule emission profiles observed in He I 10 830 Å. *Astron. Astrophys.* **472**, L51. DOI.
- Sánchez-Andrade Nuño, B., Bello González, N., Blanco Rodríguez, J., Kneer, F., Puschmann, K.G.: 2008, Fast events and waves in an active region of the Sun observed in H α with high spatial resolution. *Astron. Astrophys.* **486**, 577. DOI.
- Scharmer, G.B., Narayan, G., Hillberg, T., de la Cruz Rodríguez, J., Löfdahl, M.G., Kiselman, D., Sütterlin, P., van Noort, M., Lagg, A.: 2008, CRISP Spectropolarimetric Imaging of Penumbral Fine Structure. *Astrophys. J. Lett.* **689**, L69. DOI. ADS.
- Schmidt, W., Fisher, J.: 2013, Dynamics of the Fe II 396.94 nm emission line observed at solar disk center. *Astron. Astrophys.* **560**, A50. DOI. ADS.
- Schröter, E.H., Soltan, D., Wiehr, E.: 1985, The German solar telescopes at the Observatorio del Teide. *Vistas in Astronomy* **28**, 519. ADS.
- Scullion, E., Doyle, J.G., Erdélyi, R.: 2010, A spectroscopic analysis of macrospicules. *Mem. Soc. Astron. Italiana* **81**, 737. ADS.
- Sekse, D.H., Rouppe van der Voort, L., De Pontieu, B.: 2012, Statistical Properties of the Disk Counterparts of Type II Spicules from Simultaneous Observations of Rapid Blueshifted Excursions in Ca II 8542 and H α . *Astrophys. J.* **752**, 108. DOI. ADS.
- Sekse, D.H., Rouppe van der Voort, L., De Pontieu, B.: 2013, On the Temporal Evolution of the Disk Counterpart of Type II Spicules in the Quiet Sun. *Astrophys. J.* **764**, 164. DOI. ADS.
- Shibata, K., Suematsu, Y.: 1982, Why are spicules absent over plages and long under coronal holes. *Solar Phys.* **78**, 333. DOI.
- Shoji, M., Nishikawa, T., Kitai, R., Ueno, S.: 2010, Spectroscopic Studies of Limb Spicules. I. Radial and Turbulent Velocities. *Pub. Astron. Soc. Japan* **62**. DOI. ADS.
- Skogsrud, H., Rouppe van der Voort, L., De Pontieu, B., Pereira, T.M.D.: 2015, On the Temporal Evolution of Spicules Observed with IRIS, SDO, and Hinode. *Astrophys. J.* **806**, 170. DOI. ADS.
- Skumanich, A., Lites, B.W., Martínez Pillet, V., Seagraves, P.: 1997, The Calibration of the Advanced Stokes Polarimeter. *ApJS* **110**, 357. ADS.
- Socas-Navarro, H., Elmore, D.: 2005, Physical Properties of Spicules from Simultaneous Spectropolarimetric Observations of He I and Ca II Lines. *Astrophys. J. Lett.* **619**, L195. DOI. ADS.
- Socas-Navarro, H., Elmore, D., Pietarila, A., Darnell, A., Lites, B.W., Tomczyk, S., Hegwer, S.: 2006, Spinor: Visible and Infrared Spectro-Polarimetry at the National Solar Observatory. *Solar Phys.* **235**, 55. DOI. ADS.
- Staveland, L.: 1970, Determination of the Spread Function for Solar Stray Light. *Solar Phys.* **12**, 328. DOI. ADS.
- Stellmacher, G., Wiehr, E.: 1981, On the branching in the emission relations of Ca/+/- in prominences. *Solar Phys.* **71**, 299. DOI. ADS.
- Stellmacher, G., Wiehr, E.: 2015, Non-thermal line-broadening in solar prominences. *Astron. Astrophys.* **581**, A141. DOI. ADS.
- Stellmacher, G., Wiehr, E., Dammasch, I.E.: 2003, Spectroscopy of Solar Prominences Simultaneously From Space and Ground. *Solar Phys.* **217**, 133. ADS.
- Sterling, A.C.: 2000, Solar Spicules: A Review of Recent Models and Targets for Future Observations - (Invited Review). *Solar Phys.* **196**, 79.
- Sterling, A.C., Moore, R.L., DeForest, C.E.: 2010, Hinode Solar Optical Telescope Observations of the Source Regions and Evolution of "Type II" Spicules at the Solar Polar Limb. *Astrophys. J. Lett.* **714**, L1. DOI. ADS.
- Suematsu, Y.: 1998, Solar Spicules: A brief review of recent high-resolution observations. In: T.-D. Guyenne (ed.) *Solar Jets and Coronal Plumes, ESA Special Publication* **421**, 19.
- Suematsu, Y., Wang, H., Zirin, H.: 1995, High-Resolution Observation of Disk Spicules. I. Evolution and Kinematics of Spicules in the Enhanced Network. *Astrophys. J.* **450**, 411. DOI.
- Suematsu, Y., Shibata, K., Nishikawa, T., Kitai, R.: 1982, Numerical hydrodynamics of the jet phenomena in the solar atmosphere. *Solar Phys.* **75**, 99.
- Suematsu, Y., Katsukawa, Y., Ichimoto, K., Tsuneta, S., Okamoto, T., Nagata, S., Shimizu, T., Tarbell, T., Shine, R., Title, A.: 2007, High Resolution Observation of Spicules in Ca II H with Hinode/SOT. In: *Bulletin of the American Astronomical Society* **38**, 219.

- Suematsu, Y., Ichimoto, K., Katsukawa, Y., Shimizu, T., Okamoto, T., Tsuneta, S., Tarbell, T., Shine, R.A.: 2008, High Resolution Observations of Spicules with Hinode/SOT. In: S. A. Matthews, J. M. Davis, & L. K. Harra (ed.) *First Results From Hinode*, *ASP Conference Series* **397**, 27. ADS.
- Tandberg-Hanssen, E.: 1960, An investigation of the temperature conditions in prominences with a special study of the excitation of helium. *Astrophysica Norvegica* **6**, 161. ADS.
- Tian, H., McIntosh, S.W., De Pontieu, B., Martínez-Sykora, J., Sechler, M., Wang, X.: 2011, Two Components of the Solar Coronal Emission Revealed by Extreme-ultraviolet Spectroscopic Observations. *Astrophys. J.* **738**, 18. DOI. ADS.
- Tritschler, A., Schmidt, W., Langhans, K., Kentischer, T.J.: 2002, High-resolution solar spectroscopy with TESOS - Upgrade from a double to a triple system. *Solar Phys.* **211**, 17.
- Trujillo Bueno, J., Merenda, L., Centeno, R., Collados, M., Landi Degl'Innocenti, E.: 2005, The Hanle and Zeeman Effects in Solar Spicules: A Novel Diagnostic Window on Chromospheric Magnetism. *Astrophys. J. Lett.* **619**, L191. DOI. ADS.
- Tsiropoula, G., Schmieder, B.: 1997, Determination of physical parameters in dark mottles. *Astron. Astrophys.* **324**, 1183.
- Tsiropoula, G., Tziotziou, K., Kontogiannis, I., Madjarska, M.S., Doyle, J.G., Suematsu, Y.: 2012, Solar Fine-Scale Structures. I. Spicules and Other Small-Scale, Jet-Like Events at the Chromospheric Level: Observations and Physical Parameters. *Space Sci. Rev.* **169**, 181. DOI. ADS.
- Tsuneta, S., Ichimoto, K., Katsukawa, Y., Nagata, S., Otsubo, M., Shimizu, T., Suematsu, Y., Nakagiri, M., Noguchi, M., Tarbell, T., Title, A., Shine, R., Rosenberg, W., Hoffmann, C., Jurcevic, B., Kushner, G., Levay, M., Lites, B., Elmore, D., Matsushita, T., Kawaguchi, N., Saito, H., Mikami, I., Hill, L.D., Owens, J.K.: 2008, The Solar Optical Telescope for the Hinode Mission: An Overview. *Solar Phys.* **249**, 167. DOI. ADS.
- van Noort, M., Rouppe van der Voort, L., Löfdahl, M.G.: 2005, Solar Image Restoration By Use Of Multi-frame Blind De-convolution With Multiple Objects And Phase Diversity. *Solar Phys.* **228**, 191. DOI. ADS.
- von der Lühe, O., Soltau, D., Berkefeld, T., Schelenz, T.: 2003, KAOS: Adaptive optics system for the Vacuum Tower Telescope at Teide Observatory. In: Keil, S.L., Avakyan, S.V. (eds.) *Innovative Telescopes and Instrumentation for Solar Astrophysics, Proceedings of the SPIE* **4853**, 187. ADS.
- Watanabe, T., Steenbock, W.: 1986, Fe II emission lines in the wings of CA II H and K. I - Solar Fe II 3969.4 Å line. *Astron. Astrophys.* **165**, 163. ADS.
- Yurchyshyn, V., Abramenko, V., Goode, P.: 2013, Dynamics of Chromospheric Upflows and Underlying Magnetic Fields. *Astrophys. J.* **767**, 17. DOI. ADS.
- Zachariadis, T.G., Georgakilas, A.A., Koutchmy, S., Alissandrakis, C.E., Dara, H.C.: 1999, Fine structure of the Solar Chromosphere: Arch-Shaped Mottles. *Solar Phys.* **184**, 77.
- Zhang, Y.Z., Shibata, K., Wang, J.X., Mao, X.J., Matsumoto, T., Liu, Y., Su, J.T.: 2012, Revision of Solar Spicule Classification. *Astrophys. J.* **750**, 16. DOI. ADS.
- Zirin, H.: 1988, *Astrophysics of the sun*, Cambridge University Press, Cambridge and New York.
- Zirker, J.B.: 1962a, On the Brightness of Chromospheric Spicules. *Astrophys. J.* **135**, 515. DOI. ADS.
- Zirker, J.B.: 1962b, Spectral Observations of Solar Chromospheric Spicules. *Astrophys. J.* **136**, 250. DOI. ADS.
- Zwaan, C.: 1965, Sunspot models : a study of sunspot spectra. *Recherches Astronomiques de l'Observatoire d'Utrecht* **17**.

Appendix

A. 2D spectroscopy in H α

Figures 21 to 24 show the H α line-core images recorded with TESOS during observations Nos. 2 and 3 in setup 1. Only the unsharp-masked images are



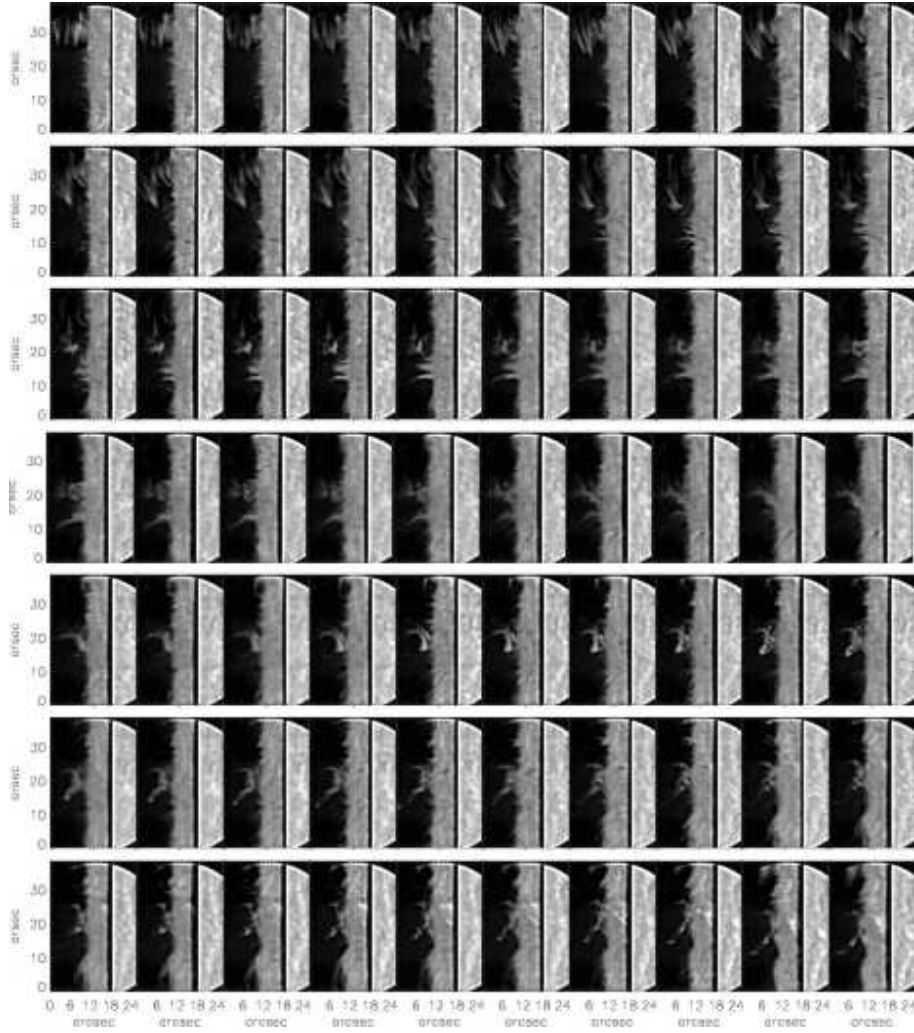


Figure 22. Second half of the time series of $H\alpha$ line-core images corresponding to observation No. 2 in Table 2. Only the image with unsharp masking is displayed. Time increases from left to right and top to bottom. The cadence between subsequent images is about 20 s.

structure with two branches. The scenery is relatively quiet all throughout the FOV before, whereas with the appearance of the large-scale structure, several individual features appear above a height of 6 Mm, affecting basically the full FOV of more than 20 Mm lateral extent at the same time. The large-scale structure is then unfortunately moved out of the FOV by the sequential scanning of the solar image by the spectrograph instruments, so the return to a relative quiet scene at the end could also be caused by this reason rather than a subsiding of the activity. The last images also show the degradation of the seeing during the observations.

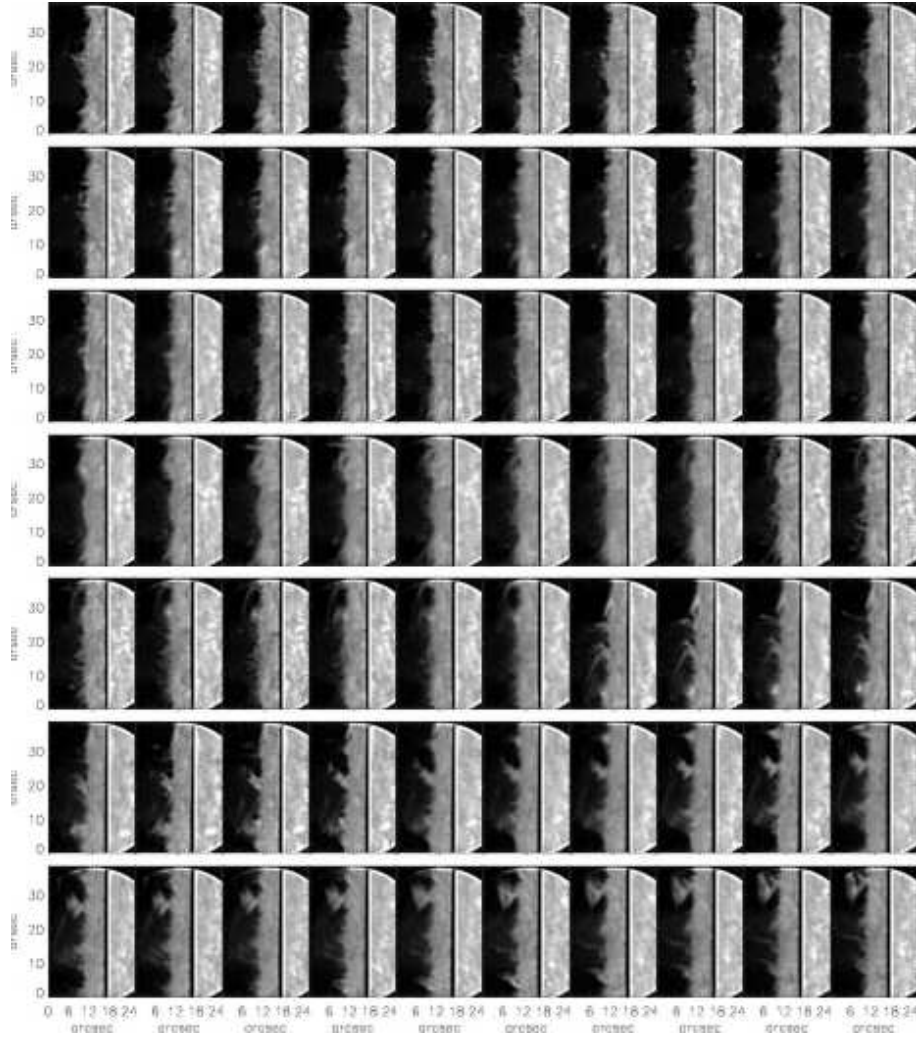


Figure 23. First part of the time series of $H\alpha$ line-core images corresponding to observation No. 3 in Table 2. Only the image with unsharp masking is displayed. Time increases from left to right and top to bottom. The cadence between subsequent images is about 20 s.

B. Limitations of Gaussian fits and significance of results

B.1. Single vs. double-Gaussian fit

The generally low light level beyond the limb, the decrease in the emission and the residuals of the stray-light correction hamper any reliable analysis. For all observations and all spectral lines, a single-Gaussian fit to all off-limb spectra was performed. All spectra with an amplitude of the Gaussian below a manually set threshold were rejected in order to remove profiles that contained only noise. To ensure that all significant profiles were kept, this threshold was set slightly

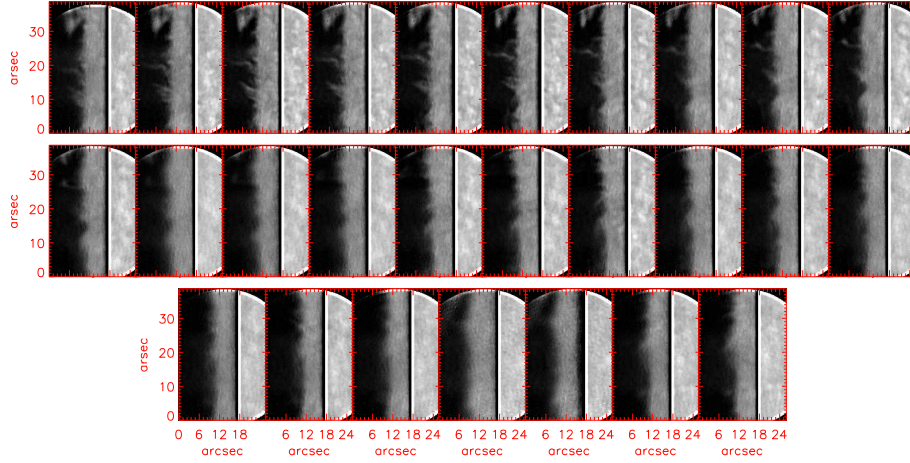


Figure 24. Second part of the time series of $H\alpha$ line-core images corresponding to observation No. 3 in Table 2. Only the image with unsharp masking is displayed. Time increases from left to right and top to bottom. The cadence between subsequent images is about 20 s.

lower than what would in principle be normal. For instance, for the He 1083 nm spectra of observation No. 1 the threshold level was chosen as 0.4 % of I_c , leading to the uniform black area in FWHM in Fig. 14, third column, bottom panel. With this initial threshold, regions with a strongly increased FWHM in the results of the single-Gaussian fit remained as being significant (Fig. 25). In the following, we investigate the corresponding profiles in more detail to show that the FWHM values derived from these profiles are spurious.

Figure 25 shows the FWHM of He 1083 nm obtained from the single-Gaussian fit for observation No. 1. We selected two vertical cuts in the spectra across a region with strongly increased FWHM at low emission (bottom row) and across a spicule with high emission (top row). The spectra along these cuts (right panels of Fig. 25) show that the emission pattern monotonically reduces both in amplitude and line width with increasing limb distance. In addition to the single-Gaussian fit, we ran a double-Gaussian fit over these profiles as well. Figure 26 shows every second individual profile along the cut of the bottom row of Fig. 25 and the corresponding Gaussian fits. It is obvious that the single-Gaussian fit is not sampling the main emission peak and gets far too broad at about pixel No. 75 (towards smaller numbers). The double-Gaussian fit performs significantly better, but the true emission amplitude for profiles below about No. 69 is difficult to assess because it is comparable to the residual amplitude of, e.g., the photospheric lines.

The individual components of the double-Gaussian fit are shown in Fig. 27. One component (green lines) samples the emission peak, while the other captures some broad offset from zero that does not correspond to the blue component of the He emission pattern. For the case of the red emission component, the line width varies around 80 pm with no clear trend (profiles 57-73), with a slight increase relative to the profiles No. 75-79. The variation comes, however, with the caveat of above: because of the limitations of the data it is not obvious which part of the emission is genuine or spurious.

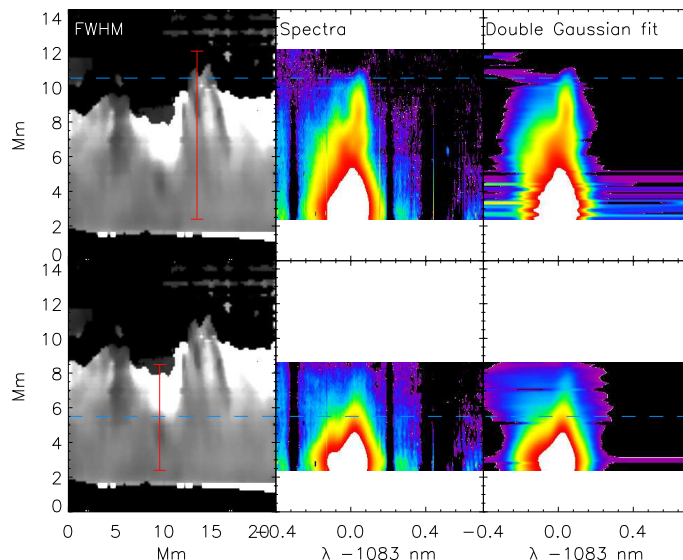


Figure 25. Quality of double-Gaussian fits. Left: FWHM from single-Gaussian fit. The red vertical bars mark the spatial location of the spectra shown in the other columns. The horizontal blue dashed lines denote the maximum extent where the fits are deemed significant and reliable. Right two columns: spectra and double-Gaussian fits along the red bars in the left column. The values are displayed on a logarithmic scale, clipped and in false color to highlight the shape at the lowest intensities.

Figure 28 shows the FWHM for both the single and double-Gaussian fits applied to the spectra selected in Fig. 25. The substantial increase in line width in the single-Gaussian fit can be seen to be fully spurious for the first cut. It is represented by the second, broad component of the double-Gaussian fit that fits the continuum offset. Otherwise the FWHM for the main emission component in the double-Gaussian fit stays roughly constant with a slight reduction in the case of the cut along the spicule.

Given the limitations of the data and the analysis as discussed above, we thus find the strong increase in FWHM in the He 1083 nm spectra – and likewise also the other lines because the line shapes are similar at some height – to be spurious. In case of low-amplitude profiles, the Gaussian fits might be more misleading than a direct look at the corresponding profiles (Figs. 4, 7, 8, 11, 12, 18, 19 and 25). The latter reveals a decrease in line width up to the point where residuals of photospheric blends are as strong as the chromospheric emission.

B.2. Influence of the blue component at 1082.91 nm

The He line at 1083 nm consists of two main components at nearby wavelengths at 1082.91 nm and 1083.03 nm (see, for instance, Sánchez-Andrade Nuño *et al.* 2007). The ratio of the two components I_{blue}/I_{red} is about 8 in the optical thin case, but can decrease to 3 at a height of about 2 Mm above the limb before approaching the optically thin case again at larger limb distances (Sánchez-Andrade Nuño *et al.* 2007, their Fig. 4). Figure 29 shows that the influence of the

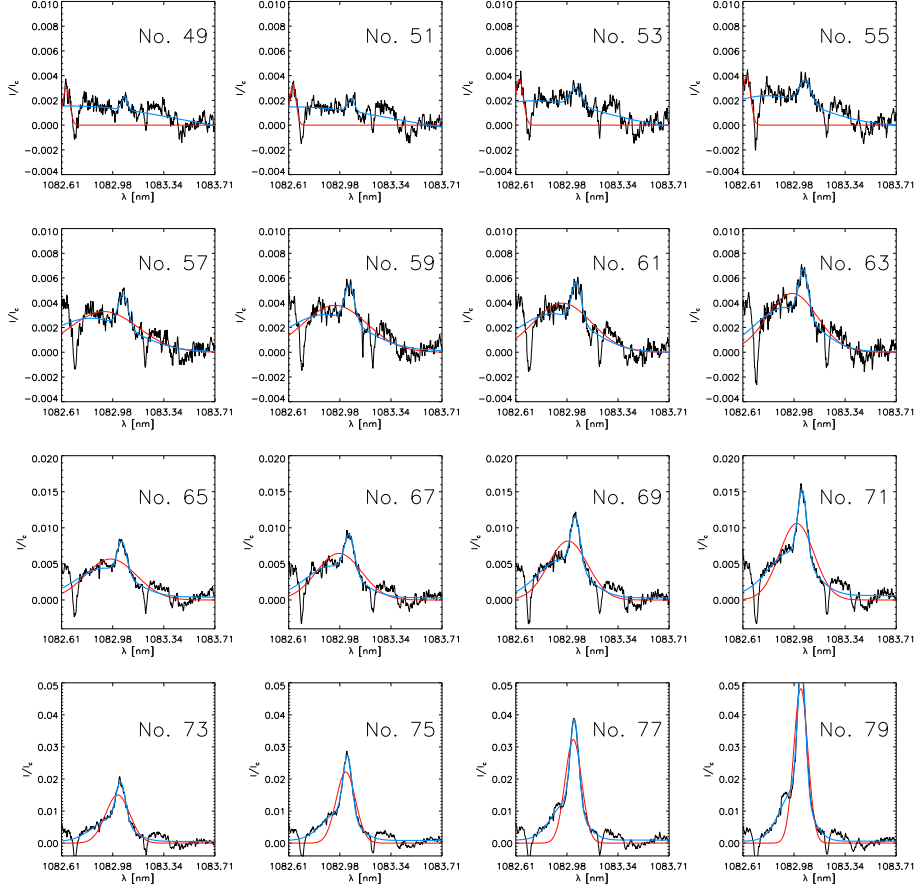


Figure 26. Gaussian fits to individual spectra. The observed spectra along the red bar in the lower row of Fig. 25 are shown with black lines. Red/blue lines show the results of the single/double-Gaussian fits. The two components of the double-Gaussian fit are shown separately in Fig. 27. The single-Gaussian fit works up to about pixel No 73. Decreasing numbers indicate increasing limb distance.

weaker blue component on the fit of the red component with a single Gaussian is minor, opposite to the residuals from the stray-light correction discussed in the previous section for profiles with a low light level far from the limb. The line width of the stronger red component of the spectra is well recovered by the single-Gaussian fit for all profiles closer to the limb than $d < 6$ Mm (profiles No. 80 or more in Fig. 29; emission amplitude 5% or more). The weaker blue component has little effect on the fit because of its much smaller amplitude. The different amplitude of the components justifies the use of only a single Gaussian for the automated analysis of the spectra across the FOV even if the He line consists of multiple components.

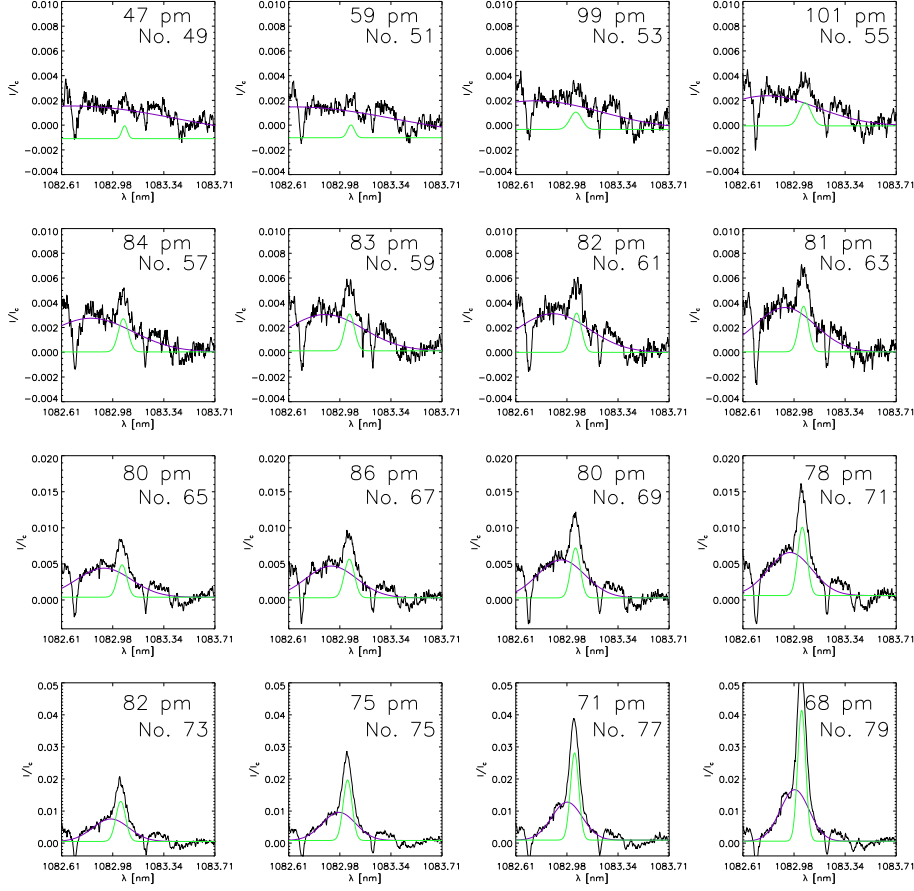


Figure 27. Double-Gaussian fit to individual spectra. The observed spectra along the red bar in the lower row of Fig. 25 are shown with black lines. Green/purple lines show the two components of the double-Gaussian fit. The values at the upper-right corner in each panel give the FWHM of the main (green) component.

C. Observations Nos. 2-4

The top panel of Fig. 30 shows the results of the Gaussian fit to the Ca II H and He I spectra of observation No. 2. This observation was selected because of its long integration time of 60 s that allows one to trace also features of very low intensities. The corresponding H α line-core images in Figs. 21 and 22 show that during this scan a large-scale (width and height of $\sim 4\text{ Mm} \times 13\text{ Mm}$) structure with a complex temporal evolution moved across the FOV. The slit-spectrograph data captured in this case nothing of the temporal evolution, but only the sheer height extent of the structure up to 13 Mm above the limb. Thanks to the long integration time, even the spectra far away from the limb could still be reliably analyzed. The plot of FWHM in the bottom panel of Fig. 30 confirms the visual impression of the top panel that the FWHM in Ca II H is

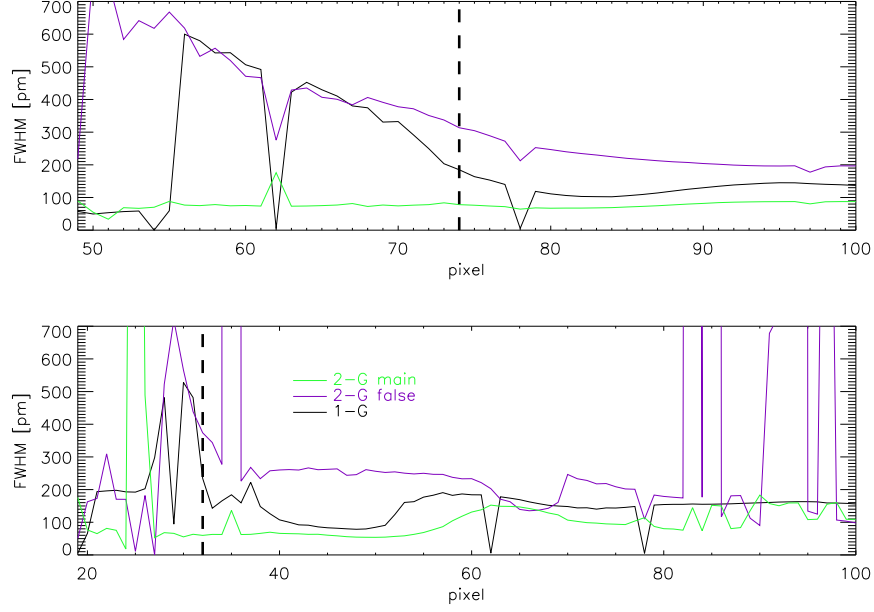


Figure 28. Comparison of FWHM from single and double-Gaussian fits. Top/bottom panel: FWHM of the spectra shown in the bottom/top row of Fig. 25. Black lines: single-Gaussian fit. Green line: main component of double-Gaussian fit. Purple line: spurious component of double-Gaussian fit (see Fig. 27). The vertical black dashed lines denote the maximum extent where the fits are deemed significant and correspond to the blue lines in Fig. 25.

monotonically decreasing up to the top of the feature. Above about $y \sim 8$ Mm, the feature presumably is the only one existing at that height, so the monotonic decline of the FWHM should not indicate a possible reduction of the overlap of different features along the LOS. For He I at 1083 nm, the FWHM shows a rise at the top, but in the corresponding maps of He I line-core intensity or the amplitude of the Gaussian, the intensity above 11 Mm is virtually zero.

The top panel of Fig. 31 shows the results of the Gaussian fit to the Ca II H and He I spectra of observation No. 3, while the corresponding H α line-core images are shown in Figs. 23 and 24. Similar to observation No. 3, the H α line-core images exhibit mainly complex-shaped structures without much resemblance to spicules at heights larger than 5 Mm above the limb. None of these features are captured in the Ca II H spectra that basically drop to zero intensity everywhere throughout the FOV above that height (top row of Fig. 31), whereas the He I spectra still sampled them up to about 10 Mm above the limb. The FWHM of Ca II H shows a rather uniform decrease with height above the limb. The FWHM of the He I line at 1083 nm shows again a basically lateral structuring with little vertical variation. On the location used for a vertical cut in the He I spectra, the FWHM decreases monotonically up to about 10 Mm above the limb (bottom panel of Fig. 31).

The last example of the 2010 data (observation No. 4, Fig. 32) was taken with the slit oriented parallel to the limb that is located just at the bottom border of

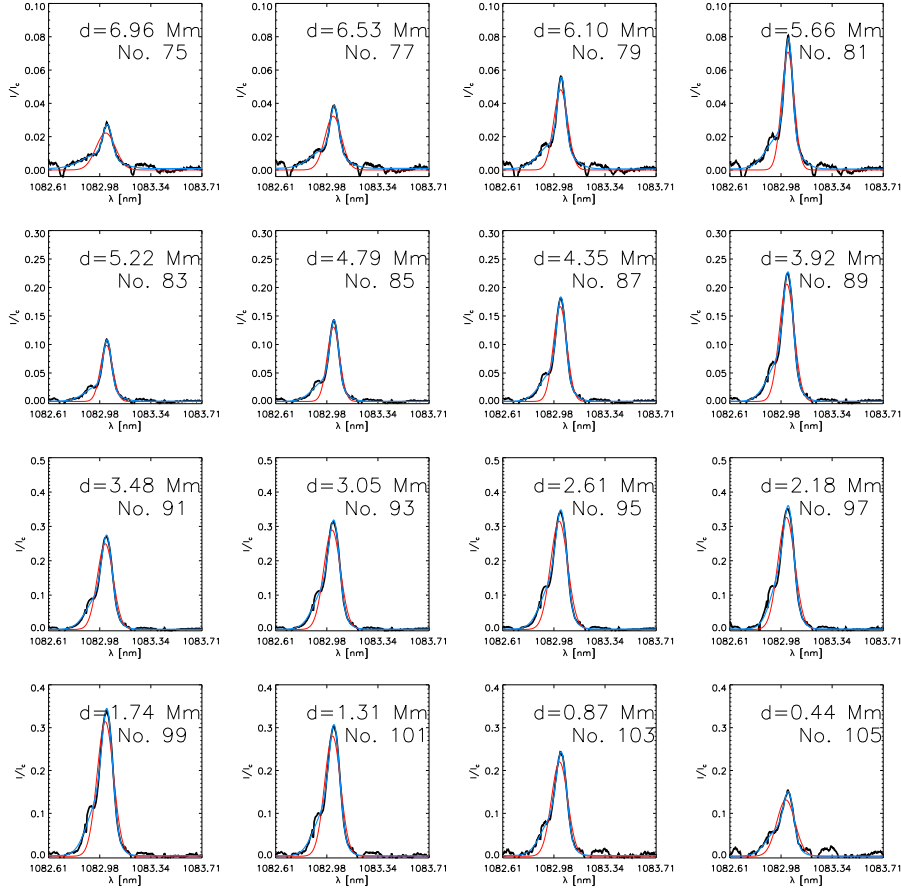


Figure 29. Gaussian fits to individual He I 1083 nm spectra from the limb to a height of about 7 Mm. The observed spectra are shown with black lines. Red/blue lines show the results of the single/double-Gaussian fits. The limb distance d is given at the top in each panel.

the FOV. We could not apply any correction for stray light to these data because of the limited extent of the FOV that neither contains a sufficiently large on-disc region nor a suitable off-limb area for calculating an average profile to be used in the stray-light correction. A few features can be called distinguishable (at $x \sim 20, 28$ and 33 Mm) in the line-core image or the intensity of the H_{2V} emission peak. The temporal evolution of their FWHM shows no indication for a significant change of the FWHM with time or height above the limb within the limitations of cadence and spatial resolution.

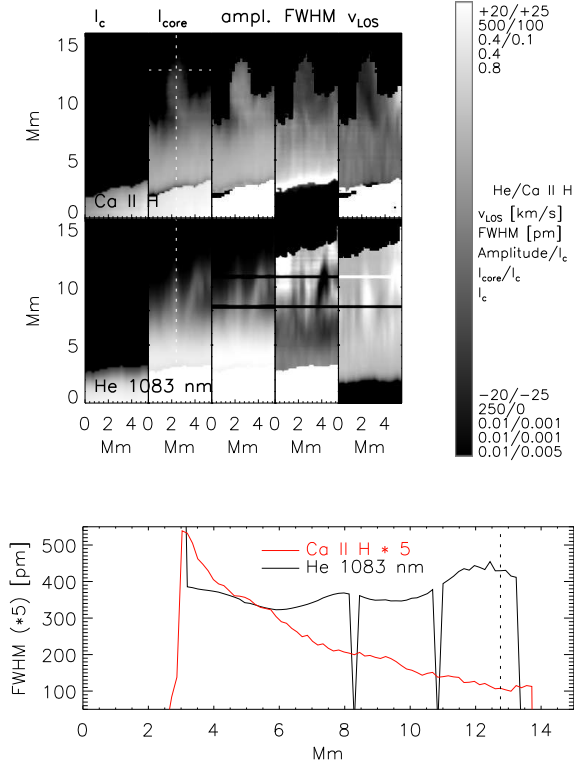


Figure 30. Top panel: results of the Gaussian fit in Ca II H and He I at 1083 nm for observation No. 2 with a 60-s integration time. Bottom panel: FWHM in Ca II H and He I at 1083 nm along the vertical dotted line in the top panel. The horizontal dotted line in the top panel and the vertical dotted line the bottom panel denote the maximal range with spectra above the noise level.

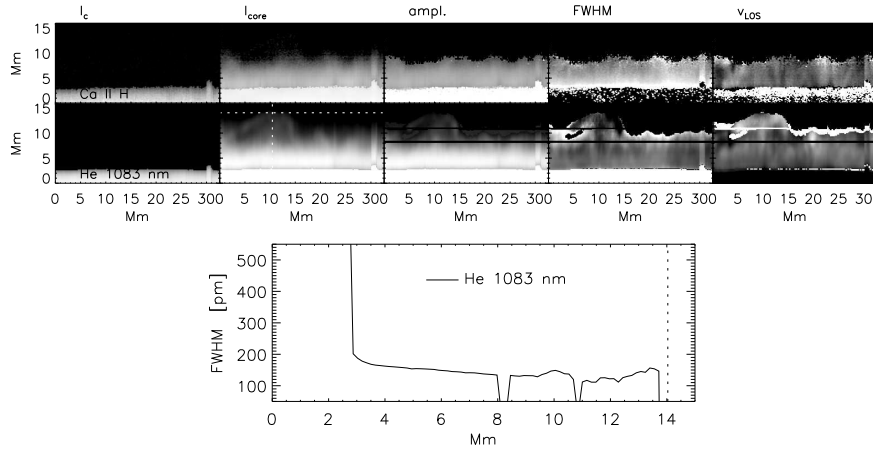


Figure 31. Top: results of the Gaussian fit in Ca II H and He I at 1083 nm for observation No. 3. Bottom: FWHM in He I at 1083 nm along the vertical dotted line in the top panel. The horizontal dotted line in the top panel and the vertical dotted line the bottom panel denote the maximal range with spectra above the noise level. For the display ranges see the grey bar of Fig. 30.

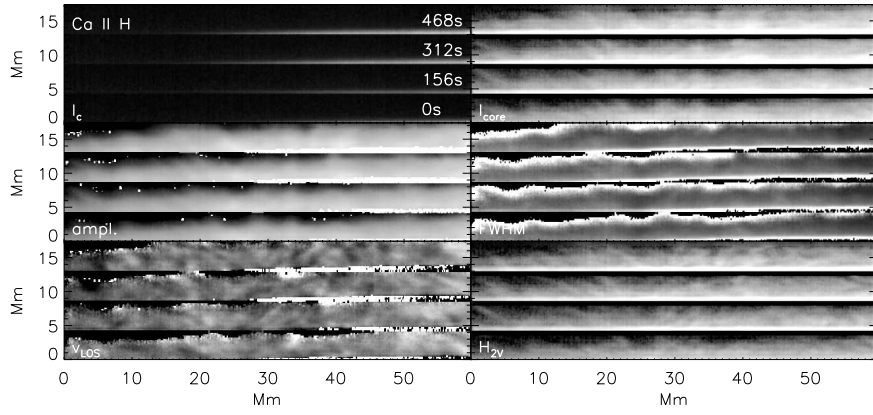


Figure 32. Results of the Gaussian fit in Ca II H for observation No. 4. Left column, top to bottom: continuum intensity, amplitude and LOS velocity. Right column, top to bottom: line-core intensity, FWHM and intensity of the H_{2V} emission peak. Note that here x corresponds to the direction along the slit and y to the scanning direction, opposite to the previous figures. The four panels in y for each quantity correspond to four repetitions of the scan taken with a cadence of 156 s. Display ranges similar as in Fig. 30.